J. Fluid Mech. (1991), *vol.* 229, *pp.* 229–268
Printed in Great Britain

Experiments on ripple instabilities. Part 3. Resonant quartets of the Benjamin–Feir type

By MARC PERLIN† AND JOE HAMMACK
Department of Aerospace Engineering, Mechanics and Engineering Sciences, University of Florida, Gainesville, FL 32611, USA

(Received 12 July 1990 and in revised form 10 January 1991)

Instabilities and long-time evolution of gravity–capillary wavetrains (ripples) with moderate steepnesses ($\epsilon < 0.3$) are studied experimentally and analytically. Wavetrains with frequencies of $8 \leqslant f \leqslant 25$ Hz are generated mechanically in a channel containing clean, deep water; no artificial perturbations are introduced. Frequency spectra are obtained from *in situ* measurements; two-dimensional wavenumber spectra are obtained from remote sensing of the water surface using a high-speed imaging system. The analytical models are inviscid, uncoupled NLS (nonlinear Schrödinger) equations: one that describes the temporal evolution of longitudinal modulations and one that describes the spatial evolution of transverse modulations.

The experiments show that the evolution of wavetrains with sensible amplitudes and frequencies exceeding 9.8 Hz is dominated by modulational instabilities, i.e. resonant quartet interactions of the Benjamin–Feir type. These quartet interactions remain dominant even for wavetrains that are unstable to resonant triad interactions ($f > 19.6$ Hz) – if selective amplification does not occur (see Parts 1 and 2). The experiments further show that oblique perturbations with the same frequency as the underlying wavetrain, i.e. rhombus-quartet instabilities, amplify more rapidly and dominate all other modulational instabilities. The inviscid, uncoupled NLS equations predict the existence of modulational instabilities for wavetrains with frequencies exceeding 9.8 Hz, typically underpredict the bandwidth of unstable transverse modulations, typically overpredict the bandwidth of unstable longitudinal modulations, and do not predict the dominance of the rhombus-quartet instability. When the effects of weak viscosity are incorporated into the NLS models, the predicted bandwidths of unstable modulations are reduced, which is consistent with our measurements for longitudinal modulations, but not with our measurements for transverse modulations.

Both the experiments and NLS equations indicate that wavetrains in the frequency range 6.4–9.8 Hz are stable to modulational instabilities. However, in these experiments, wavetrains with sensible amplitudes excite one of the members of the Wilton ripples family. When second-harmonic resonance occurs, both the first- and second-harmonic wavetrains undergo rhombus-quartet instabilities. When third-harmonic resonance occurs, only the third-harmonic wavetrain undergoes rhombus-quartet instabilities.

---

† Present address: Department of Naval Architecture and Marine Engineering, University of Michigan, Ann Arbor, MI 48109, USA.

1. Introduction

Gravity–capillary wavetrains (ripples) on a water surface exhibit a variety of instabilities. For wavetrains with moderate amplitudes, these instabilities and typical scales can be identified using the inviscid dispersion relation for an infinitesimal wavetrain:

$$c^2 := \frac{\omega^2}{k^2} = \frac{g}{k}(1+\tau)\tanh kh; \tag{1a}$$

$$\tau = \frac{Tk^2}{\rho g}. \tag{1b}$$

In (1), ω is the radian frequency, g is the gravitational force per unit mass, ρ is the mass density, T is the surface tension, h is the quiescent water depth, k is the magnitude of the wave vector, c is the wave celerity defined in terms of these parameters, and τ is a reciprocal Bond number that may be interpreted as the ratio of surface tension and gravitational energies. These energies are equal ($\tau = 1$) for a wavetrain whose cyclic frequency is $f = \omega/2\pi = 13.6$ Hz and wavelength is $\lambda = 2\pi/k = 1.7$ cm. (Herein we assume that $T = 73$ dyn/cm and $kh \gg 1$; both are applicable to our experiments.) In general, we can define ripples as those waves in a range, say, from $\tau = 0.1$ ($f = 5.6$ Hz and $\lambda = 5.4$ cm) to $\tau = 10$ ($f = 56$ Hz and $\lambda = 0.54$ cm) so that gravity waves occur for $\tau < 0.1$ and capillary waves occur for $\tau > 10$. An important instability of ripples was investigated by Wilton (1915) who found that internal resonances occur for a countable family of wavetrains corresponding to

$$\tau = 1/n \quad (n = 2, 3, \ldots). \tag{2}$$

According to (1) and (2), Wilton $n = 1/\tau$ ripples have the same speed as their nth harmonic. For example, Wilson $n = 2$ ripples ($\tau = 0.5$) correspond to a wavetrain whose frequency is 9.8 Hz. This wavetrain can be viewed as a degenerate case of a more general class of instabilities resulting from resonant three-wave interactions. Both the Wilton $n = 2$ ripples and resonant triad interactions were reviewed and investigated in Part 1 of this series (Henderson & Hammack 1987); a further investigation is presented in Part 2 (Perlin, Henderson & Hammack 1990). According to RIT (resonant interaction theory), a wavetrain's frequency must exceed 19.6 Hz ($\tau = 2$) before it becomes unstable to background waves through resonant triad interactions. (Second-harmonic resonance is the exceptional case.) Wavetrains with frequencies below 19.6 Hz can first be destabilized by resonant four-wave interactions. Resonant quartet interactions can occur when the wave vectors $\boldsymbol{k} = (l, m)$ and frequencies ω of four infinitesimal wavetrains satisfy the kinematical conditions:

$$\boldsymbol{k}_1 \pm \boldsymbol{k}_2 = \boldsymbol{k}_3 \pm \boldsymbol{k}_4, \tag{3a}$$

$$\omega_1 \pm \omega_2 = \omega_3 \pm \omega_4. \tag{3b}$$

Theoretical investigation of resonant quartets is tiresome, owing to straightforward but tedious algebra when solving (3) and when deriving the evolution equations; reviews are given by Phillips (1977) and Craik (1985). Degenerate cases are somewhat easier to analyse, and they are especially important in the evolution of our experimental wavetrains. An example that occurs in the experiments is third-harmonic resonance (Wilton $n = 3$ ripples) corresponding to an 8.37 Hz wavetrain. The wave vectors in this quartet are collinear, and in (3) we take $f_1 = f_2 = f_3 = 8.37$ Hz, $f_4 = 25.11$ Hz, $k_1 = k_2 = k_3 = 2.12$ rad/cm, $k_4 = 6.36$ rad/cm, and choose

appropriate signs. Another example that dominates most of our experiments involves two wave-vector pairs, which sum according to (3*a*) to form a nearly collinear, nearly rhombus parallelogram, i.e.

$$\boldsymbol{k}_1 = \boldsymbol{k}_3 =: \boldsymbol{k}, \tag{4a}$$

$$\boldsymbol{k}_2 = \boldsymbol{k}_4 =: \boldsymbol{k} + \delta\boldsymbol{k}, \tag{4b}$$

where $\delta\boldsymbol{k} = (\delta l, \delta m)$ is the modulational wave vector with $\delta k \ll k$, and

$$\omega_1 = \omega_3 =: \omega, \tag{4c}$$

$$\omega_2 = \omega_4 =: \omega + \delta\omega, \tag{4d}$$

where $\delta\omega$ is the modulational frequency with $\delta\omega \ll \omega$. Hence, this quartet comprises only two identifiable wavetrains that interact collinearly when there are no transverse modulations ($\delta m = 0$), and interact obliquely when there are transverse modulations ($\delta m \neq 0$).

Studies of degenerate quartet interactions described by (4) have focused on the evolution of a single wavetrain $(\boldsymbol{k}_1, \omega_1)$ interacting with a continuum of smaller-amplitude, second waves with modulational wavenumbers and frequencies. Lighthill (1965), Benjamin & Feir (1967), Whitham (1967) and Zakharov (1968) conducted the seminal studies of this type for collinear gravity wavetrains and discovered their instability to longitudinal modulations. (Hereinafter, we refer to instabilities resulting from either transverse or longitudinal modulations as BF (Benjamin–Feir) instabilities.) Dynamical equations for the evolution of BF instabilities have been derived by numerous investigators including Benney & Newell (1966), Benney & Roskes (1969) and Davey & Stewartson (1974) who examined gravity waves, and Djordjevic & Redekopp (1977) who examined ripples. For collinear interactions, these equations reduce to the well-known NLS (nonlinear Schrödinger) equation, which was independently derived for water waves by numerous investigators, including Zakharov (1968) and Hasimoto & Ono (1972). The NLS equation arises in many branches of physics, and it has received considerable attention since Zakharov & Shabat (1972) showed that it is completely integrable using IST (inverse scattering transforms, see e.g. Ablowitz & Segur 1981, for a review of IST). NLS equations will be exploited in the investigation presented herein.

The object of this study is to investigate the stability and long-time evolution of ripple wavetrains with moderate steepnesses in the presence of naturally occurring perturbations. The experiments motivate a review in §2 of classical results for BF instabilities of wavetrains with longitudinal modulations and an introduction of NLS equations that describe the temporal and spatial evolution of wavetrains with transverse modulations (only). We discuss theoretical predictions of these equations that are tested by our experiments, and we review predictions arising from less restrictive model equations for the long-time evolution of gravity, capillary and ripple wavetrains. We also discuss the modifications of the inviscid NLS models due to weak viscosity. In §3 we describe the laboratory apparatus and practices with special emphasis on a high-speed imaging system that allows us to obtain quantitative measurements of wave vectors by remote sensing of the water surface. Experimental results are presented and compared with theoretical predictions in §4; a discussion of our results and conclusions are presented in §5. An epilogue is presented in §6 that summarizes our experimental observations in this three-part series of papers with an emphasis on a fundamental failure of RIT to predict, even qualitatively, the evolution of ripple wavetrains when resonant triads are dynamically possible.

2. Theoretical considerations and literature review

The discovery of a gravity wavetrain's instability to longitudinal modulations coupled with the discovery of IST and its success in solving the NLS equation have precipitated a bountiful literature. Most of this literature concerns gravity waves, though there are important exceptions that examine ripple and capillary wavetrains. In this section, we review the literature in order to explain our experimental measurements of ripples (§4) and contrast their behaviour with that of gravity and capillary wavetrains. (Detailed reviews can be found in Yuen & Lake 1982 and Craik 1985.) First, we review NLS equations with an emphasis on their underlying approximations. Secondly, we introduce the models that are applied to our experiments. Thirdly, we discuss the limitations of NLS equations for modelling the long-time evolution of wavetrains and review results from less restrictive, and presumably better, models. Finally, a discussion of viscous effects is presented with special emphasis on the reduction in the bandwidths of unstable modulations.

2.1. *The NLS equations and modulational instabilities*

Consider a water layer that is bounded above by a free surface with uniform tension, bounded below by an impermeable, rigid solid, and unbounded in lateral extent. Water motions are references to a right-handed Cartesian coordinate system $0x'y'z'$ with the (x', y')-plane embedded in the quiescent free surface and the z'-axis pointing upward, opposite gravity. The inviscid irrotational motions are describable in terms of a harmonic velocity potential $\phi(x', y', z', t')$ and the (related) vertical deformation $\eta(x', y', t')$ of the water surface from its quiescent position. The unknowns satisfy nonlinear boundary conditions (Lamb 1932, §110), which make the water-wave problem analytically intractable. Here, we are interested in approximate solutions that embody the properties of (4), i.e. a small-amplitude wavetrain that is nearly monochromatic and nearly one-dimensional. Further, we assume that the wavetrain has a characteristic amplitude a_0 and propagates mainly in the x'-direction. In order to make these approximations explicit, we introduce three small parameters of the same order:

$$\epsilon := a_0 k = O\left(\frac{|m|}{k}\right) = O\left(\frac{\delta k}{k}\right) \ll 1, \tag{5}$$

where the wave steepness ϵ measures nonlinearity, $|m|/k$ measures two-dimensionality, and $\delta k/k$ measures the modulational wavenumber bandwidth. We also require $(kh)^2 \gg \epsilon$ to avoid shallow water. Using expansions for ϕ and η and standard perturbation methods, the first-order solution for the infinitesimal wavetrain is:

$$\phi(x', y', z', t') = \epsilon\left(\frac{\cosh k(z'+h)}{\cosh kh}[A'\,\mathrm{e}^{\mathrm{i}\theta} + A'^*\,\mathrm{e}^{-\mathrm{i}\theta}] + \Phi'\right), \tag{6}$$

$$\eta(x', y', t') = \epsilon(a\,\mathrm{e}^{\mathrm{i}\theta} + a^*\,\mathrm{e}^{-\mathrm{i}\theta}), \tag{7}$$

in which

$$\theta = kx' - \omega t', \tag{8}$$

ω is given by the dispersion relation of (1), Φ' is a constant at this order and (*) denotes complex conjugate. The complex amplitude a of the wavetrain is related to the complex amplitude of the velocity potential by

$$a = \left(\frac{\mathrm{i}\omega}{g + k^2 T}\right) A'. \tag{9}$$

To determine higher-order effects we use the method of multiple scales and introduce slow spacescales and timescales ($\epsilon x', \epsilon y', \epsilon t', \epsilon^2 t'$; see Ablowitz & Segur 1981). Carrying out the expansions to second order, i.e. $O(\epsilon^2)$, we obtain the well-known results that envelope modulations propagate with the energy speed U of an infinitesimal wavetrain, i.e.

$$U = \frac{\mathrm{d}\omega}{\mathrm{d}k} = \tfrac{1}{2}c\left(\frac{1+3\tau}{1+\tau} + \frac{2kh}{\sinh 2kh}\right), \tag{10}$$

and induce a mean flow given by $\nabla\Phi'$. In order to proceed to third order, we view the motion in dimensionless envelope coordinates:

$$x = \epsilon k(x' - Ut'), \quad y = \epsilon k y', \quad t = \epsilon^2 \omega_0 t', \tag{11a–c}$$

$$A = k^2/\omega_0 A', \quad \Phi = k^2/\omega_0 \Phi', \tag{11d, e}$$

where $\omega_0 = (gk)^{\frac{1}{2}}$. Carrying out the expansions we find that A and Φ satisfy the following equations:

$$\mathrm{i}A_t + \zeta A_{xx} + \mu A_{yy} = \chi|A|^2 A + \chi_1 \Phi_x A, \tag{12a}$$

$$\beta\Phi_{xx} + \Phi_{yy} = -\beta_1(|A|^2)_x, \tag{12b}$$

where the (real) coefficients are given by

$$\zeta = \left(\frac{k^2}{2\omega_0}\right)\frac{\mathrm{d}^2\omega}{\mathrm{d}k^2} = \frac{\omega}{4\omega_0}\left[\frac{2\tau}{1+\tau} - 1 - \frac{4\tau^2}{(1+\tau)^2} - \frac{4(kh)^2\cosh 2kh}{\sinh^2 2kh}\right] + \frac{\omega}{2\omega_0}\left(\frac{U}{c}\right)^2, \tag{13a}$$

$$\mu = \frac{kU}{2\omega_0} \geqslant 0, \quad \sigma = \tanh kh, \tag{13b, c}$$

$$\chi = \frac{\omega_0}{4\omega}\left[\frac{(1-\sigma^2)(9-\sigma^2)+\tau(3-\sigma^2)(7-\sigma^2)}{\sigma^2-\tau(3-\sigma^2)} + 8\sigma^2 - 2(1-\sigma^2)^2(1+\tau) - \frac{3\sigma^2\tau}{1+\tau}\right], \tag{13d}$$

$$\chi_1 = 1 + \frac{kU}{2\omega}(1-\sigma^2)(1+\tau) \geqslant 0, \quad \beta = \frac{(gh-U^2)}{gh}, \tag{13e, f}$$

$$\beta_1 = \frac{\omega}{\omega_0 kh}\left[\frac{kU}{\omega}(1-\sigma^2) + \frac{2}{1+\tau}\right] \geqslant 0. \tag{13g}$$

The derivation of (12) outlined above closely follows Ablowitz & Segur (1979, 1981, §4.3*b*). (A misprint in the numerator of the first bracketed term of (13*d*) for the coefficient χ in their expression has been corrected.) Similar equations for ripples were derived by Djordjevic & Redekopp (1977); equations of this form for gravity waves were obtained by Benney & Roskes (1969) and Davey & Stewartson (1974). Unfortunately, (12) does not appear to be solvable using IST over the full range of parameters for which it remains a valid model (Ablowitz & Segur 1979).

2.1.1. *Evolution of wavetrains with longitudinal modulations*

When transverse variations are neglected in (12), i.e. $\partial_y = 0$, the equations for the mean flow and envelope velocity potential decouple to yield the evolution equations:

$$\mathrm{i}A_t + \zeta A_{xx} = \psi|A|^2 A, \tag{14a}$$

$$\Phi_x = -(\beta_1/\beta)|A|^2, \quad \psi = \chi - \chi_1\beta_1/\beta. \tag{14b, c}$$

Equation (14*a*) is the NLS equation; it was first derived by Benney & Newell (1966), Zakharov (1968) and Hasimoto & Ono (1972); and it was shown to be completely

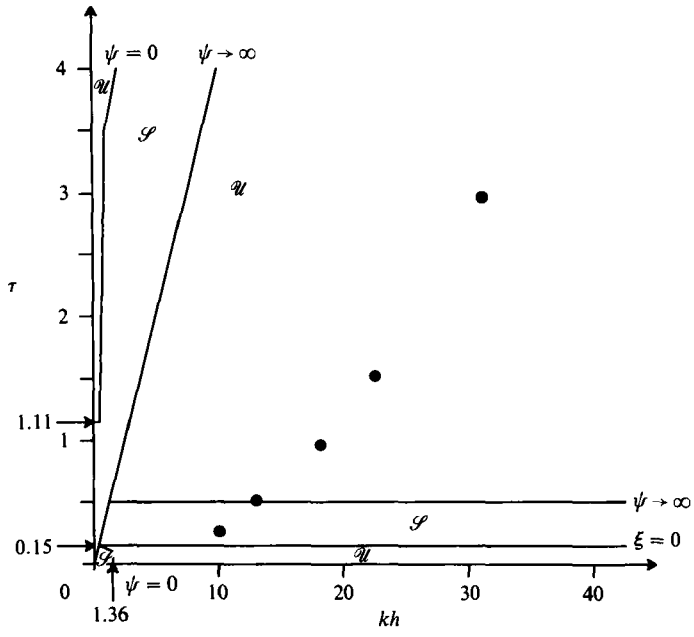

FIGURE 1. Map of parameter space for the nonlinear Schrödinger equation showing regions of stability $\mathscr{S}$ and instability $\mathscr{U}$ of a wavetrain to longitudinal modulations. ●, location of an experiment.

integrable using IST by Zakharov & Shabat (1972). In particular, Hasimoto & Ono (1972) used (14*a*) to study the onset and evolution of the longitudinal Benjamin–Feir instability of gravity wavetrains. A wavetrain's stability depends on the sign of the coefficient product $\zeta\psi$, with $\zeta\psi < 0$ for instability. Regions of stability and instability are best presented using a map of parameter space that shows curves across which sign changes in the product $\zeta\psi$ occur. Figure 1 is an extension of the map presented by Djordjevic & Redekopp (1977) and Ablowitz & Segur (1981, p. 321). Regions of stability ($\mathscr{S}$) and instability ($\mathscr{U}$) to longitudinal modulations are indicated. The classical instability of gravity ($\tau = 0$) waves for $kh > 1.36$ (Whitham 1967) occurs in consequence of a simple zero in the coefficient ψ. As surface tension, or τ, increases for $kh > 1.36$, wavetrains remain unstable until a simple zero in ζ occurs at $\tau = 0.155$, corresponding to a wavetrain whose frequency is 6.4 Hz when $T = 73$ dyn/cm. Wavetrains then remain stable until $\tau = 0.5$ (Wilton $n = 2$ ripples) where a singularity in ψ (actually in χ) occurs. Wavetrains are unstable for further increases in surface tension (or frequency) until another singularity in ψ (due to a zero in β) is encountered. This singularity corresponds to a long-wave, short-wave resonance discussed by Djordjevic & Redekopp (1977). For larger τ, wavetrains become stable once more before a final region of instability occurs when another simple zero of ψ is encountered.

Figure 1 also shows the location of our experiments that include wavetrains with five different frequencies. Table 1 summarizes theoretical parameters, which are based on infinitesimal amplitudes, for these five wavetrain frequencies. According to figure 1 and the parameters listed in table 1, three experimental wavetrains are expected to be unstable to longitudinal modulations, one is expected to be stable, and one (Wilton $n = 2$ ripples) is not predicted since it lies on a singular boundary of parameter space.

ω (rad/s)	ω_0 (rad/s)	k (rad/cm)	λ (cm)	c (cm/s)	U (cm/s)	kh	τ	ζ	$-\psi$	$-\hat{\chi}$	k_ν† (rad/cm)	γ_ν† (rad/s)	e_ν† (cm)	$\lvert A_0 \rvert$
57.1	78.8	6.33	0.99	24.8	31.0	31.1	2.98	0.685	0.223	0.073	6.42	2.87	10.8	0.
06.8	66.9	4.56	1.38	23.4	25.9	22.5	1.55	0.476	0.485	0.237	4.63	1.70	15.2	0.
85.5	60.2	3.69	1.70	23.2	23.2	18.2	1.00	0.358	1.025	0.658	3.75	1.23	18.9	0.
31.6	50.3	2.58	2.43	23.8	19.9	12.7	0.50	—	—	—	2.62	0.73	27.1	-
50.3	44.2	1.99	3.16	25.3	18.3	9.8	0.29	—	—	—	2.02	0.51	36.1	-

† Viscous calculations use $\nu = 0.01$ cm^2/s.

LE 1. Theoretical parameters for experimental wavetrains based on infinitesimal amplitudes with $h = 4.92$ cm and $T = 73$

Quantitative information for unstable modulations was obtained from (14a) by Hasimoto & Ono (1972) who noted that this equation has nonlinear plane envelope solutions of the form

$$A(x,t) = A_0 \exp(\mathrm{i}(\kappa x - \Omega t)), \tag{15a}$$

which satisfy the envelope dispersion relation

$$\Omega = \zeta\kappa^2 + \psi|A_0|^2, \tag{15b}$$

with $\zeta > 0$ and $\psi < 0$ for the unstable case. Using these solutions, they examined the Stokes' wavetrain ($\kappa = 0$) perturbed by collinear wavetrains and found an unstable band of modulational wavenumbers,

$$0 < |\kappa| < |A_0|(-2\psi/\zeta)^{\frac{1}{2}} =: K, \tag{16a}$$

as well as the most-unstable wavenumber, κ_m, and its initial temporal growth rate, γ_m:

$$|\kappa_m| = |A_0|(-\psi/\zeta)^{\frac{1}{2}} = \frac{K}{\sqrt{2}}, \quad \gamma_m = -\psi|A_0|^2. \tag{16b, c}$$

These results reconfirmed and extended earlier results for the BF instability. The parameters ζ and ψ, which depend only on properties of the underlying infinitesimal wavetrain, are listed in table 1 for each unstable wavetrain frequency in our experiments. For subsequent comparison with experimental data, we also note that the (dimensional) most-unstable longitudinal wavelength Λ_x and its e-folding distance e_x are given by

$$\Lambda_x = \frac{2\pi}{\kappa_m k}, \quad e_x = \frac{U}{\gamma_m \omega_0}, \tag{17a, b}$$

and that the (dimensional) amplitude, a_0, of the wavetrain is related to the (dimensionless) envelope amplitude, A_0, according to

$$|A_0| = \frac{\omega k a_0}{2\omega_0 \tanh kh}. \tag{17c}$$

2.2.2. *Evolution of wavetrains with transverse modulations*

When longitudinal variations are neglected in (12), i.e. $\partial_x = 0$, the equations for the mean flow and envelope velocity potential decouple to yield the evolution equations:

$$\mathrm{i}A_t + \mu A_{yy} = \chi|A|^2 A, \tag{18a}$$

$$\Phi_{yy} = 0. \tag{18b}$$

While (18a) is mathematically equivalent to (14a), the wave motion described is quite different. The wavetrain still propagates in the x-direction; however, only transverse modulations, which result from obliquely interacting wavetrains, occur. The stability of the wavetrain to these oblique wavetrains depends on the sign of the coefficients' product, with instability occurring for $\mu\chi < 0$. Since $\mu \geqslant 0$, there is only one curve in parameter space, which corresponds to the singularity in χ for Wilton $n = 2$ ripples. Since $\chi < 0$ for $\tau > 0.5$, all wavetrains with $f > 9.8$ Hz on clean, deep water are unstable to transverse modulations. Hence, the inviscid, uncoupled NLS equations (14a) and (18a), which are approximations to (12), predict that our

experimental wavetrains with frequencies exceeding 9.8 Hz are unstable to both longitudinal and transverse modulations, while our experimental wavetrains with frequencies below 9.8 Hz are stable to both.

Motivated by experimental observations, we introduce dimensionless coordinates and write (18*a*) in laboratory coordinates to obtain:

$$X := kx', \quad Y := ky', \tag{19}$$

$$\mathrm{i}\left(A_t + \frac{Uk}{\omega_0} A_X\right) + \mu A_{YY} = \chi |A|^2 A. \tag{20}$$

The experiments show that envelopes of the wavefields are (quasi-) steady in laboratory coordinates during timescales appropriate to the NLS equation. Assuming steady motion, our primary model equation for studying the stability of ripple wavetrains with transverse modulations is:

$$\mathrm{i}A_X + \hat{\mu} A_{YY} = \hat{\chi} |A|^2 A, \tag{21a}$$

in which

$$\hat{\mu} = \frac{\omega_0}{Uk}\mu = 0.5, \quad \hat{\chi} = \frac{\omega_0}{Uk}\chi. \tag{21b, c}$$

Again, (21*a*) is mathematically equivalent to (14*a*) and (18*a*), but represents a different physical situation that is more commonly found in diffraction studies; it describes the spatial evolution of the transverse modulations in laboratory coordinates. Following Hasimoto & Ono (1972), nonlinear plane envelope solutions of (21*a*) with the form

$$A(Y, X) = A_0 \exp(\mathrm{i}(qY - pX)), \tag{22a}$$

have a dispersion relation

$$p = \hat{\mu} q^2 + \hat{\chi} |A_0|^2. \tag{22b}$$

The band of unstable transverse modulational wavenumbers is

$$0 < |q| < |A_0| \left(-2\frac{\hat{\chi}}{\hat{\mu}}\right)^{\frac{1}{2}} = |A_0| (-4\hat{\chi})^{\frac{1}{2}} =: Q, \tag{23a}$$

while the most unstable transverse wavenumber q_m and its initial (spatial) growth rate Γ_m are:

$$|q_m| = |A_0| (-\hat{\chi}/\hat{\mu})^{\frac{1}{2}} = |A_0| (-2\hat{\chi})^{\frac{1}{2}} = Q/\sqrt{2}, \quad \Gamma_m = -\hat{\chi} |A_0|^2. \tag{23b, c}$$

The parameter $\hat{\chi}$, which depends only on properties of the underlying infinitesimal wavetrain, is listed in table 1 for each unstable wavetrain frequency in our experiments. The (dimensional) most unstable transverse wavelength Λ_y and its *e*-folding distance e_y are given by

$$\Lambda_y = \frac{2\pi}{q_m k}, \quad e_y = \frac{1}{\Gamma_m k}. \tag{24a, b}$$

We note from (17*b*) and (24*b*) that $e_x \approx e_y$ for deep water as in our experiments (see table 3). Hence, uncoupled NLS equations suggest that the most unstable longitudinal and transverse modulations grow at equal (spatial) rates. We also note that the transverse instability leads to a directional spreading of wave energy within angles of $\pm\theta_{\mathrm{E}}$ from the direction of the wave vector of the underlying wavetrain; this angle is given by

$$\theta_{\mathrm{E}} = \arctan(Q). \tag{25}$$

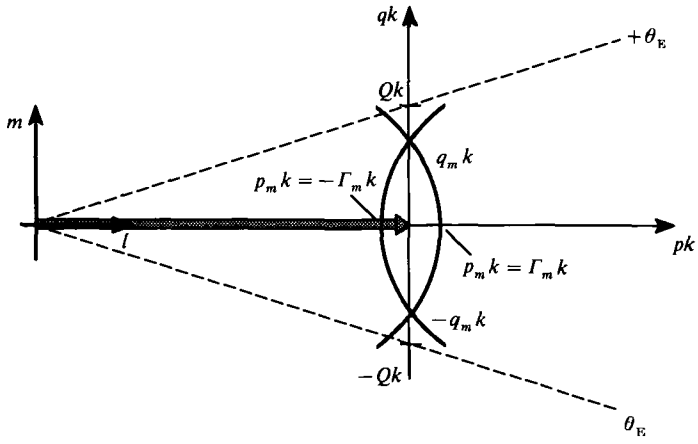

FIGURE 2. Schematic drawing (not to scale) of wavenumber space illustrating the directional spread of energy (amplitude) of a wavetrain (dotted arrow) owing to unstable transverse modulational wavenumbers (solid line).

Theoretical results for the transverse spatial instability are illustrated in figure 2, which shows the dimensional wavenumber plane, (l, m), with a wave-vector in the l-direction that represents the underlying wavetrain. Both branches of the dispersion curves (parabolas) for the envelope modulations of (22b) are shown in the dimensional (pk, qk)-plane whose origin is at the tip of the input wave vector. Only the portions of these branches within the unstable transverse wavenumber band are shown. Note that the longitudinal wavenumber $p_m k$, which corresponds to the most unstable transverse modulation q_m, is zero, whereas a wavetrain with no transverse modulation, i.e. $qk = 0$, has a small longitudinal wavenumber equal to the spatial growth rate $\Gamma_m k$, which is also the longitudinal wavenumber for $qk = Qk$ at the edge of the unstable band. (These longitudinal modulations are the spatial frequencies of the plane envelope solutions, analogous to the temporal frequency Ω in (15b).) Wavenumber spectra measured in the experiments for wavetrains with $f > 9.8$ Hz are expected to show energy (or amplitude) along the unstable branches of the dispersions curves shown in figure 2.

Another property of the plane envelope solutions of (22a) is their spatial phase speed, c_e, which is referenced to laboratory coordinates, and is found from the dispersion relation of (22b) to be

$$c_e := p/q = \hat{\mu} q + \hat{\chi}/q |A_0|^2. \tag{26}$$

A trajectory of constant phase in the (Y, X)-plane will lie on a straight line with a slope

$$\mathrm{d}Y/\mathrm{d}X = c_e \tag{27}$$

so that it forms an angle with the X-axis given by

$$\theta_s := \arctan(c_e). \tag{28}$$

Using (23), (26) and (28) we find that lines of constant phase have the following angles for the range of unstable transverse wavenumbers:

$$\theta_s \to \tfrac{1}{2}\pi \quad \text{as} \quad q \to 0, \tag{29a}$$

$$\theta_s \to 0 \quad \text{as} \quad q \to q_m. \tag{29b}$$

Of particular interest in the experiments are envelope nodal lines that are distinctive features of the observed wave pattern; they appear as 'striations'. According to (29), these striations can occur at any angle up to 90°; however, if the pattern is dominated by the most unstable wavenumber, the striations should be parallel to the wave-channel axis. When striations occur, these results allow us to estimate the associated transverse wavenumber, say q_s, based on the striation angle, which is easily measured from a photograph of the surface wave pattern. From (26) and (28) we find that

$$q_s = \pm(\tan\theta_s \pm (\tan^2\theta_s + 2\Gamma_m)^{\frac{1}{2}}), \tag{30}$$

where the root(s) must be chosen so that the narrow-band approximation of (5) is not violated.

2.2. *Long-time evolution of wavetrains*

The long-time evolution of periodic wavetrains that are modulationally unstable has received considerable study (see Yuen & Lake 1982, or Craik 1985, for reviews). Nevertheless, definitive predictions for either gravity, gravity–capillary, or capillary wavetrains remain elusive. Analytical insight is especially difficult, even from weakly nonlinear models such as the NLS equation, since IST is not easily extended to periodic initial data. Numerical studies of the NLS equation for gravity waves (Yuen & Ferguson 1978) and experiments (Lake *et al.* 1977) showed the existence of modulational and demodulational cycles that lead to near recurrence of the original wavetrain. Ma (1979) used IST and the NLS equation to examine the evolution of wave envelopes that decay to a uniform (non-zero) constant at infinity, and he found an unsteady soliton solution that is also suggestive of recurrence. Martin & Yuen (1980) examined gravity wavetrains with oblique perturbations using a two-dimensional NLS equation

$$\mathrm{i}A_t + \zeta A_{xx} + \mu A_{yy} = \chi|A|^2 A, \tag{31}$$

which is the deep-water limit ($kh \to \infty$) of (13). (Equation (31) was first derived by Zakharov (1968); according to Ablowitz & Segur (1981, §3.7), it is not solvable by IST.) Martin & Yuen found an unbounded band of unstable wavenumbers that allows energy leakage to large wavenumbers. This leakage prevents recurrence, but more importantly, high wavenumbers violate the narrow-band approximation that underlies (31). Once this shortcoming was discovered, attention turned to less restrictive models that remain applicable for larger modulational wavenumbers and larger wavetrain nonlinearities. Here, we summarize results from these other models for gravity, capillary, and ripple wavetrains.

2.2.1. *Gravity wavetrains*

Crawford *et al.* (1981) exploited an integro-differential equation of Zakharov (1968) to study longitudinal and transverse modulations of gravity wavetrains of moderate amplitudes. For longitudinal modulations, they found that higher-order nonlinear effects reduce the growth rates and bandwidth of unstable wavenumbers. For oblique interactions, the Zakharov equation predicts that the band of unstable wavenumbers is bounded and that the most unstable modulations are longitudinal. Extensive numerical computations using the Zakharov equation (see Yuen & Lake 1982, and the references cited therein) show a variety of long-time behaviours that depend on wavetrain nonlinearity, the distribution of unstable modes, and the number of modes included in the calculations. As wavetrain nonlinearity increases, behaviour ranges from recurrence to chaos; however, at sufficiently large amplitudes, which exceed the putative range of validity of the Zakharov equation, the wavetrain stabilizes, i.e. the

band of unstable wavenumbers vanishes. The existence of neutrally stable perturbations gives rise to the possibility of bifurcated solutions, which were found for gravity waves using the Zakharov equation by Saffman & Yuen (1980*a*, *b*) and Ma (1982*a*).

McLean *et al.* (1981) and McLean (1982*a*, *b*) examined the stability of large-amplitude gravity wavetrains to oblique perturbations. They found a class of instabilities (resonant quintets, termed class II), first noted by Longuet-Higgins (1978) in one dimension, whose most unstable wave vector is always oblique, similar to two-dimensional bifurcated solutions. These class II instabilities dominate Benjamin–Feir instabilities (termed class I), which disappear for large amplitudes. They also found neutrally stable perturbations, which suggest the possibility of bifurcated solutions. Meiron, Saffman & Yuen (1982) confirmed the existence of bifurcated solutions using Euler's equations; these results were extended by Chen & Saffman (1985). Experimental evidence of bifurcated solutions and BF instabilities among deep-water gravity waves was presented by Melville (1982), Su (1982) and Su *et al.* (1982).

2.2.2. *Capillary and ripple wavetrains*

Chen & Saffman (1985) examined the stability of capillary wavetrains on deep water using (31) as well as Euler's equations. Their results showed that small-amplitude wavetrains are most unstable to oblique perturbations; however, large-amplitude wavetrains are most unstable to collinear perturbations. Neutrally stable perturbations also occur at large amplitudes, and bifurcated solutions were obtained. Hogan (1985) used the Zakharov equation and the narrow-band approximation to derive a fourth-order equation for the evolution of modulated ripple wavetrains. Hogan's fourth-order results predict a larger band of unstable wavenumbers than at third-order. Hogan also showed that the band of third-order modulationally stable waves, i.e. $0.155 < \tau < 0.50$ (see figure 1), remains stable at fourth order.

Chen & Saffman (1979, 1980) examined one-dimensional bifurcations of ripple wavetrains that include Wilton ripples. These results were extended to two-dimensions by Ma (1982*b*) using the Zakharov equation. Zhang & Melville (1987) investigated the stability of large-amplitude ripples with $\tau > 2$, and found instabilities occurring in the neighbourhood of linear triad, quartet, and quintet resonance curves. They also found that BF instabilities disappear for ripple wavetrains with moderate amplitudes, but reappear for large amplitudes. The wave vector of the most unstable wavetrain is generally oblique, though not always. Neutrally stable perturbations were also found.

Henderson (1986) conducted ripple experiments for wavetrains with frequencies of 5, 13.5, and 15 Hz, and concluded that only one resonant quartet was excited: a degenerate quartet consisting of two waves with the same frequency and wavenumber magnitude so that their wave vectors formed a rhombus. (We find that her conclusion is essentially correct; however, we also show that a continuum of rhombus quartets are amplified and that this process is predicted (somewhat) by a NLS equation.)

2.3. *Viscous effects*

All of the theoretical models described above neglect fluid viscosity, ν; nevertheless, viscous effects can be significant for fluid motions with the lengthscales of ripples and capillary waves. In §3 and in Part 1, fairly elaborate precautions are described for minimizing viscous effects arising at the water surface in our experimental facility. In spite of these precautions, Henderson & Lee (1986) showed that the viscous

damping of our experimental waves is predicted well by a model that assumes the surface is inextensible (Lamb 1932, §§349–351). According to this weak-viscosity model, thin Stokes' (laminar) boundary layers give rise to a viscous attenuation of wave amplitudes and to a viscous dispersion relation. For deep, wide channels, as in our experiments, the damping rate γ_ν and its e-folding distance e_ν are given by

$$\gamma_\nu = (\tfrac{1}{8}\nu k_\nu^2 \omega_\nu)^{\frac{1}{2}} = U/e_\nu, \tag{32a, b}$$

where

$$\omega_\nu = (gk_\nu(1 + Tk_\nu^2/\rho g)^{\frac{1}{2}}, \tag{32c}$$

and k_ν is the viscous wavenumber. Viscosity decreases wavelengths in our experiments; thus, the actual (viscous) wavenumber is larger than its inviscid counterpart in (1). (The wavetrain's frequency $\omega = 2\pi f$ is fixed by the wavemaker motion.) The viscous wavenumber is found from the viscous dispersion relation

$$2\pi f = \omega_\nu - \gamma_\nu. \tag{33}$$

Once k_ν is determined from (33), the damping coefficient and its e-folding distance can be found; results are shown in table 1. Note that the largest viscous increase in wavenumber is 0.09 rad/cm, which is about 1% of the inviscid value and smaller than our measurement resolution (0.284 rad/cm, see §3.2). Hence, viscous effects on dispersion are not expected to be important in the experiments. The e-folding distances listed in table 1 correspond to about ten wavelengths for each experimental frequency. Since the locations of our wavenumber measurements are about one or two e-folding distances downstream of the wavemaker, viscous attenuation of wave amplitudes is expected to be important in the experiments.

Miles (1984) noted that the consequences of weak (linear) viscous effects, such as those described above, are incorporated into nonlinear evolution equations for the envelope amplitude by letting

$$\partial/\partial t \to \partial/\partial t + \delta_1, \quad \partial/\partial x \to \partial/\partial x + \delta_2, \tag{34a, b}$$

in the inviscid NLS equations (14a) and (21a), respectively. The damping rates $\delta_{1,2}$ in (34) are given by

$$\delta_1 = \gamma_\nu/\omega_0, \quad \delta_2 = \gamma_\nu/Uk. \tag{35a, b}$$

The viscous nonlinear Schrödinger equations become

$$\mathrm{i}A_t + \mathrm{i}\delta_1 A + \mu A_{yy} = \chi|A|^2 A, \quad \mathrm{i}A_X + \mathrm{i}\delta_2 A + \hat{\mu} A_{YY} = \hat{\chi}|A|^2 A. \tag{36a, b}$$

Repeating the linear stability analyses of Hasimoto & Ono (1972) using (36a, b) and using (34a, b) in the evolution equations that are obtained for the perturbations, we find that the bandwidths of unstable (viscous) wavenumbers are reduced according to

$$\tfrac{1}{2}K^2(1-(1-\delta_1^2/\gamma_m^2)^{\frac{1}{2}}) < |\kappa_\nu| < \tfrac{1}{2}K^2(1+(1-\delta_1^2/\nu_m^2)^{\frac{1}{2}}), \tag{37a}$$

$$\tfrac{1}{2}Q^2(1-(1-\delta_2^2/\Gamma_m^2)^{\frac{1}{2}}) < |q_\nu| < \tfrac{1}{2}Q^2(1+(1-\delta_2^2/\Gamma_m^2)^{\frac{1}{2}}). \tag{37b}$$

Hence, only those modulations with wavenumbers in the inviscid bands of (16a) and (23a) having inviscid growth rates exceeding the viscous damping rates can amplify. In addition, the amplitude of the primary wavetrain must exceed a minimum (threshold) value before modulations amplify. The threshold amplitudes corresponding to longitudinal and transverse modulations are

$$|A_0|^L_{\nu\text{-min}} = \left(\frac{\delta_1}{(-\psi)}\right)^{\frac{1}{2}}, \quad |A_0|^T_{\nu\text{-min}} = \left(\frac{\delta_2}{(-\hat{\chi})}\right)^{\frac{1}{2}}. \tag{38a, b}$$

These threshold amplitudes are shown in table 1 for each of our experimental wavetrains that is predicted to be unstable by the NLS equations.

3. Experimental facilities, data analyses, lighting and image calibration

The experimental facilities consist of the following: (i) wave tank, (ii) wavemaker, (iii) wave gauge, (iv) water supply and filters, (v) computer, and (vi) high-speed imaging system. Items (i)–(iv) were described in detail by Henderson & Lee (1986) and Henderson & Hammack (1987, Part 1); therefore, the descriptions herein are brief. Item (v) was described in detail and item (vi) was described briefly by Perlin *et al.* (1990, Part 2). Here we describe the imaging system and image calibration techniques more thoroughly. We also describe our algorithms for calculating frequency spectra from temporal wave gauge data and two-dimensional wavenumber spectra from spatial images.

A schematic drawing of the wave tank and other apparatus is shown in figure 3. The wave tank is 91 cm wide, 183 cm long, and 15 cm deep; it has tempered glass sidewalls and bottom, which are in an aluminium frame with aluminium endwalls. This frame also supports a positioning system for an instrument carriage over the tank. A sheet of white Plexiglas is attached to the underside of the glass bottom. The tank is supported by a steel frame that rests on vibration-isolation pads. Temporary wave guides, made of (wetted) aluminium, are set into the tank to create a wave channel whose breadth is 30.5 cm and length is 91 cm.

A wavemaker is located at one end of the wave channel. The paddle is supported by an electrodynamical shaker, which is connected to a steel frame that straddles the wave tank and is attached to the laboratory floor through isolation pads (see figure 3). The paddle is an aluminium right-angled wedge that spans the wave channel; its cross-section has a height of 0.90 cm and width of 0.44 cm as shown by the inset of figure 3(*a*). For an experiment, the paddle is immersed 0.24 cm in the water and oscillates vertically about this position with a stroke amplitude s, which is listed in table 2 for each experiment. (It is crucial for experimental repeatability that the immersion depth of the paddle be maintained.) An eddy-current displacement transducer measures the vertical motion of the paddle and provides position feedback to a servo-controller, which compares the feedback with the command signal for desired paddle motion and provides an appropriate drive signal to the electrodynamical shaker.

A capacitance wave gauge is used to measure the water surface elevation as a function of time at a fixed location in the wave channel. The water-penetrating probe is a sealed glass tube, which encloses a conductor; the tube's diameter is 1.17 mm. The gauge's frequency response remains constant until about 30 Hz and attenuates thereafter. Dynamical calibrations of the gauge are performed as described in Part 1.

The water supply contains about 80 gal. of doubly distilled water stored in two closed polyethylene crocks that are connected to the wave tank and a filtration system by PVC piping and valves, and by Tygon tubing. The Sybron filtration system includes a 0.2 μm particle filter, a carbon-absorption filter, and an organics filter. Water is gravity-fed into the wave tank before experiments to a depth of 4.92 cm, which is established using a point gauge (see figure 3). Afterwards, the water is pumped through the filtration system and into the storage crocks. Our procedures consistently produce a water surface in the tank whose static surface tension, measured by a Du Nouy tensiometer, is 73 dyn/cm.

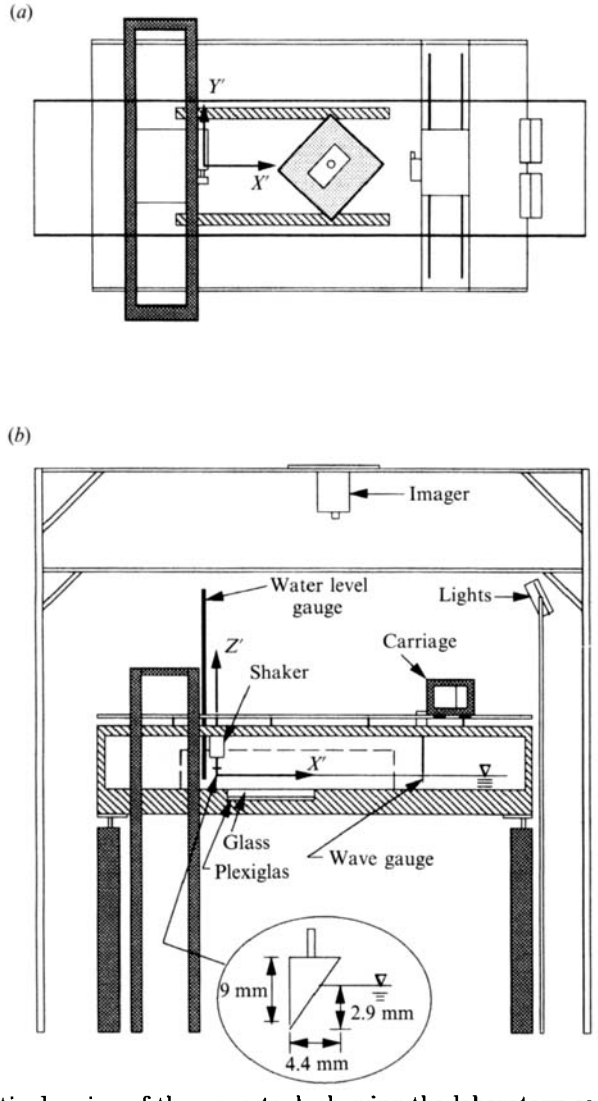

FIGURE 3. Schematic drawing of the wave tank showing the laboratory coordinate system and other apparatus. (*a*) Plan view. (*b*) Elevation view.

3.1. *Computer and high-speed imaging systems*

The computer system is a 32-bit DEC (Digital Equipment Corporation) VAXstation II equipped with 527 Mbytes of disk storage. The computer's 12-bit analog-output (AAV11-DA) system provides command signals for the wavemaker and for the dynamical calibration of the wave gauge. All sinusoidal command signals are constructed from a 2500 Hz digital output. The computer's analog-input (ADV11-DA) system acquires data from the wave gauge, feedback, and command signals. The analog-input and -output devices are supported by separate, programmable real-time clocks. Software control for these devices is provided by Signal Technology's Interactive Laboratory System and DEC's Labstar. The VAXstation II is connected to the computer of the high-speed imagining system through an RS-232 communication interface.

The Kodak Ektapro 1000 is a computer-based, high-speed video system that

provides digital images from analog signals recorded at rates of 30–1000 f.p.s. (frames per second). The analog signals comprising a frame are generated by an imager that measures light intensities using an NMOS array of 192 (rows) × 240 (columns) pixels. (Light intensities are shown to be related to wave amplitudes in §3.3.) Imager measurements are converted to FM (frequency-modulated) signals and recorded on instrumentation tape. During play-back, the FM signals are demodulated and sampled by an A/D (analog/digital) converter that provides digital images at a rate of 30 f.p.s.; light intensity at a pixel site is resolved by 256 grey levels. Digital video signals are stored in a frame buffer that can be displayed on a system monitor and/or downloaded to a standard video recorder. Each data frame is surrounded by a border that contains the frame number and other recording information; jogging among frames allows us to repeatedly access specific frames. For the experiments reported herein, the imager is located above the wave channel as indicated in figure 3(*a*). The focal plane of the imager is parallel to, and 1.5 m above the water surface; a 25 mm TV lens is used. Examples of two frames from the experiments, as viewed on a video monitor, are shown in figure 4. The first frame shows a quiescent water surface within the wave channel, which is inclined at 45° across the frame. (The black, square border superposed on the wave channel and the reason for inclining the imager relative to the channel axes will be discussed in §3.2.) The second frame in figure 4(*b*) shows the wave channel with an 8 Hz wavetrain (experiment GC0806); crests and troughs appear as light and dark bands, respectively. (A detailed description of video images is presented in §3.3.) Digital images can be transferred from the frame buffer of the Ektapro 1000 through a communication interface to the VAXstation II computer system using the Ektapro's command language. This communication link and language also allow the imaging system to be controlled by the VAXstation II.

3.2. *Data analyses*

During an experiment, we monitor the wave gauge, command, and feedback signals; herein, only data from the wave gauge are reported. Continuous-time signals from the wave gauge are low-pass (Butterworth) filtered with a cutoff frequency of 100 Hz, amplified 20 dB, high-pass filtered with a cutoff frequency of 1 Hz, amplified another 20 dB, and then sampled at a rate of 250 Hz. (A 20 dB amplification corresponds to a factor of 10; in general, log(factor) = (dB/20)). The sampling interval is 65.532 s, which yields 2^{14} (or 16384) samples in a digital time series. An amplitude-frequency spectrum is computed using an FFT (fast Fourier transform) algorithm from the ILS software; frequency resolution is 0.015 26 Hz and the Nyquist frequency is 125 Hz. Spectral amplitudes are presented in arbitrarily scaled units of dB.

Before an experiment, a short sequence of frames showing the quiescent water surface is recorded. Then the wavemaker is started, and, after 40 s, a recording of the wave field is begun; a framing rate of 125 f.p.s. is used for all experiments herein. One frame of the quiescent water surface and one frame of the wave field are then chosen for processing. From these frames, a $2^7 \times 2^7$ pixel array, which corresponds to the (22 × 22) cm surface area outlined by the square black border superposed on the image in figure 4(*a*), is analysed. The row and column spacing between pixels in this array is 0.174 cm; this spacing was measured using the imager reticle and viewing scales, which were supported at the level of the water surface. Grey level measurements from the image of the quiescent water surface are then subtracted from those at corresponding pixel sites in the wave field image. The resulting grey

(*a*)

(*b*)

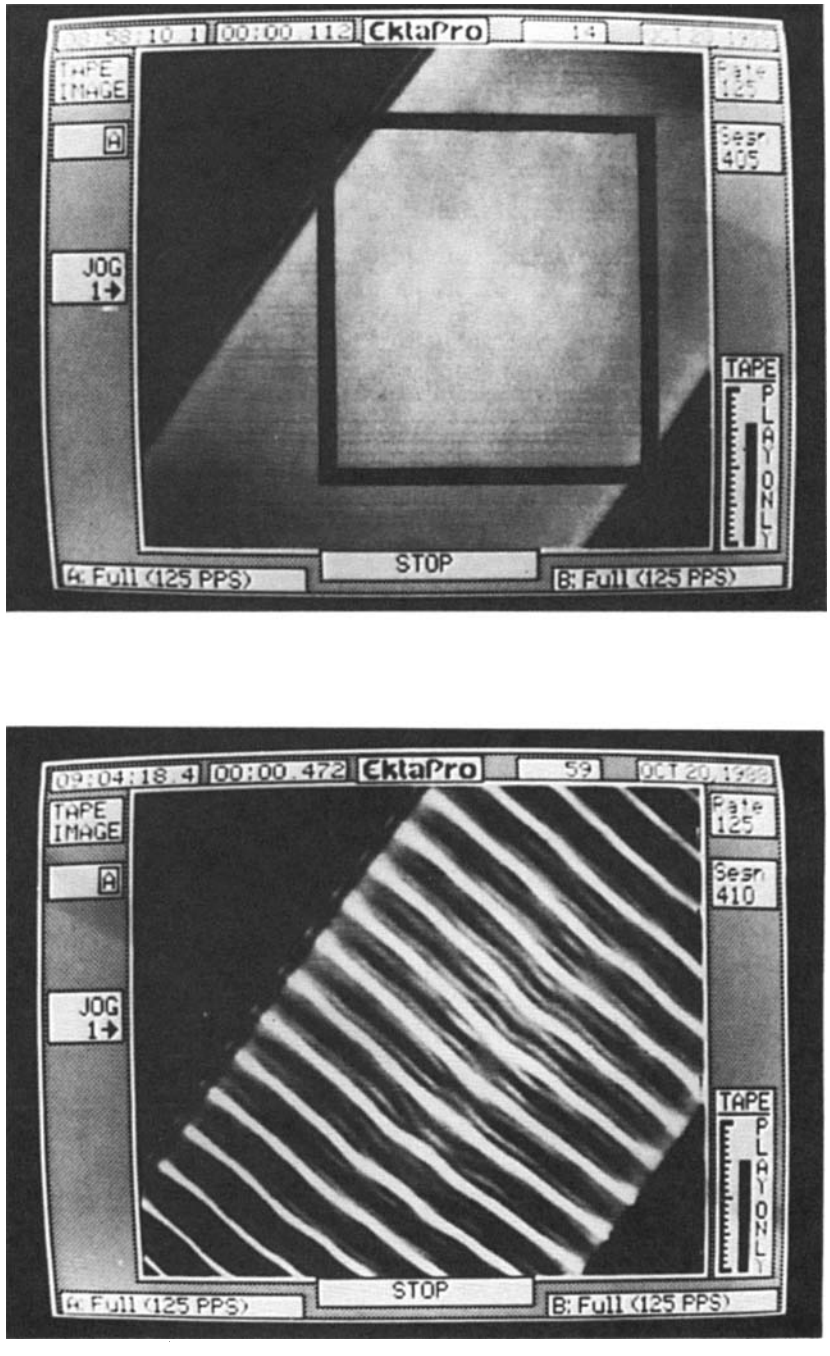

FIGURE 4. Overhead images of the wave channel viewed on the video monitor. (*a*) Quiescent water surface with superposed black square border showing spatial sampling region; (*b*) 8 Hz wavetrain from experiment GC0806. Light bands are wave crests; dark bands are wave troughs.

levels, which spanned 225 of the possible 256 in some experiments, are not affected by variations in the background lighting within an image (see §3.3) or differences in response among imager sensors. A mean value of grey levels is then computed and subtracted from each pixel site. A two-dimensional amplitude-wavenumber spectrum

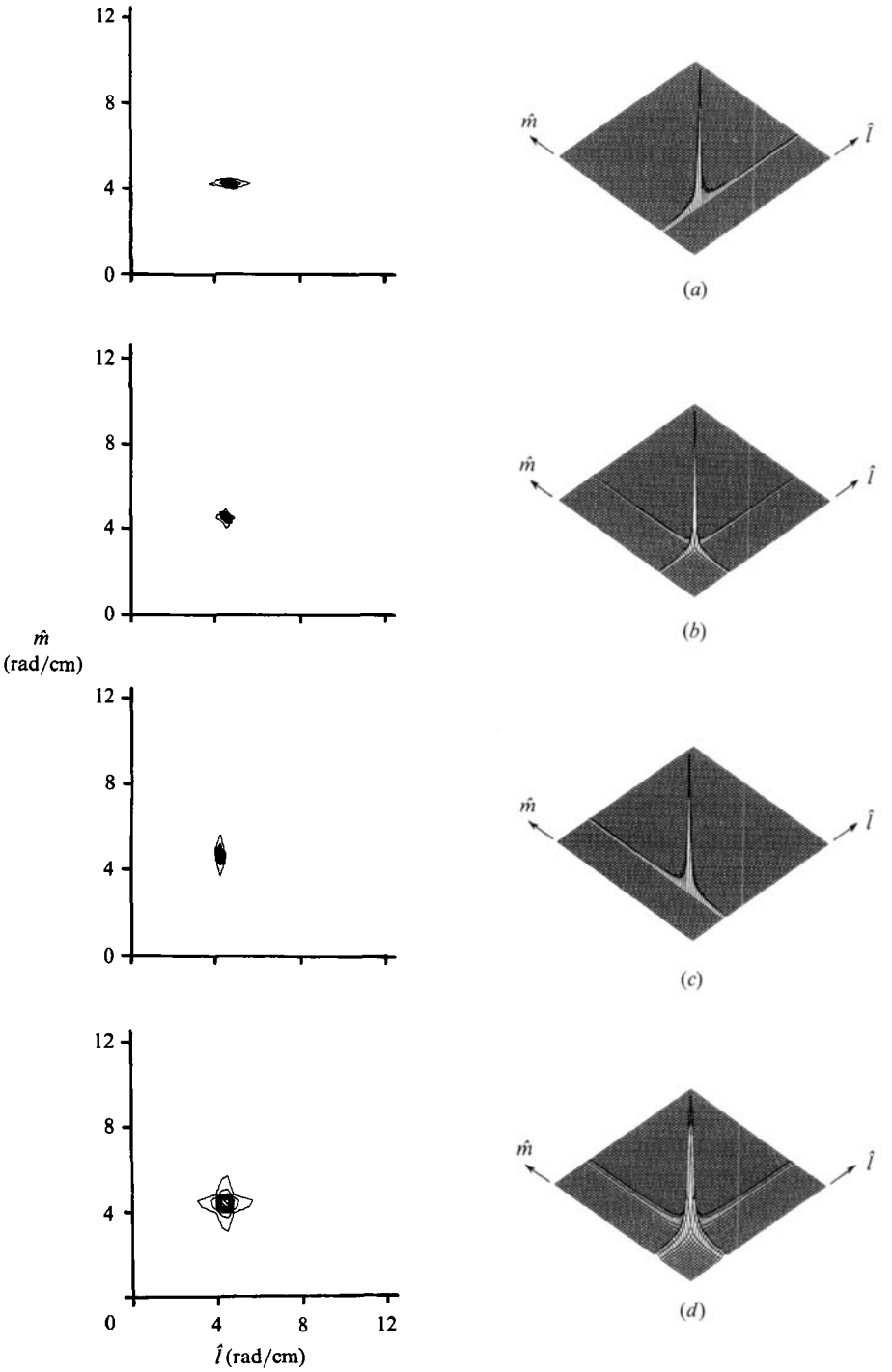

FIGURE 5. Perspective views and contour maps of two-dimensional wavenumber spectra for analytical sine waves: (*a*) $f = 25$ Hz, $\hat{k} = 6.325$ rad/cm, $\hat{\theta} = 42°$; (*b*) $f = 25$ Hz, $\hat{k} = 6.325$ rad/cm, $\hat{\theta} = 45°$; (*c*) $f = 25$ Hz, $\hat{k} = 6.325$ rad/cm, $\hat{\theta} = 48°$; (*d*) $f = 24.4$ Hz, $\hat{k} = 6.200$ rad/cm, $\hat{\theta} = 45°$.

is computed from the resulting array of grey levels using a two-dimensional FFT algorithm from the Labstar software. The wavenumber resolution in this spectrum is 0.284 rad/cm and the Nyquist wavenumber is 18.055 rad/cm, which, according to (1), corresponds to a 106.5 Hz wavetrain. Spectral amplitudes are presented in arbitrarily scaled units. We note that low-pass filtering of signals representing the spatial image is not possible – the image signal is discrete space *ab initio*. However, the lighting of the image appears to eliminate high wavenumbers, and we observed no evidence of aliasing in the computed wavenumber spectra. We also note that spatial data and wave gauge data are not obtained simultaneously, since the supporting apparatus of the wave gauge interferes with the lighting and viewing of the water surface. Hence, the control and reproducibility of our experiments are essential.

There are two other aspects of the two-dimensional wavenumber spectra that should be mentioned. First, the FFT algorithm automatically folds amplitudes for negative wavenumbers $(-l, -m)$ into the positive quadrant of wavenumber space; hence, information on wave-vector directions is restricted to 0–90°. In order to obtain information on waves propagating in the $-m$ and $+m$ directions, we rotated the imager to an angle of (about) 45°, as shown in figure 4(*a*); hence, wave directions within $\pm 45°$ of the channel axis are resolved. Wave vectors in the rotated coordinates are denoted $\hat{k} = (\hat{l}, \hat{m})$. Secondly, the two-dimensional FFT algorithm produces results using analytical sine waves that should be demonstrated before examining experimental data. Figure 5 presents perspective views and contour maps of the wavenumber spectrum for four simulations using analytical sine waves that were discretized and processed as in the experiments. The first three simulations use a sine wave with $k = 6.325$ rad/cm, which corresponds to a 25 Hz wavetrain according to (1). These wavetrains are directed at angles $\hat{\theta}$ that correspond to propagation in and near the direction of the channel axis (45°). The fourth simulation slightly decreases the wavenumber of the sine wave, and directs it along the channel axis. While all of the spectra are dominated by a peak at the input wavenumber and angle, there is a tendency for the spectral amplitude not to diminish to zero away from the peak in either the $\hat{l}$, $\hat{m}$, or both directions. Instead, a nearly constant amplitude is reached that persists and leads to elongated contours in the axial directions away from the peak. This phenomenon does not result from the finite extent of the rectangular spatial window used in our sampling; it also resulted when we used a 10% cosine (Hanning) window (e.g. see Childers & Durling 1975, p. 290). When this phenomenon occurs in both axial directions, as in figure 5(*d*), amplitude contours of the spectrum resemble a hypocycloid of four cusps. No physical significance should be assigned to this shape when it is evident in experimental results.

3.3. *Lighting and image calibration*

After much trial and error, we adopted a lighting configuration as shown in figure 3. Two 600 W halogen lights in reflector housings are positioned at the downstream end of the wave tank astride the axis of the wave channel and about 60 cm above the water surface. (The wavemaker paddle is located 1.4 m from the downstream tank endwall.) The lights are aimed at the imaged area so that the incident light forms an angle of about 32° with the normal to the water surface. The opaque (white) Plexiglas located on the underside of the tank bottom provides reflected diffuse light that is measured by the imager over the wave channel. This diffuse light is refracted by the deformed water surface so that wave crests and troughs appear in the images as light and dark bands, respectively. Figure 6 presents quantitative evidence that the

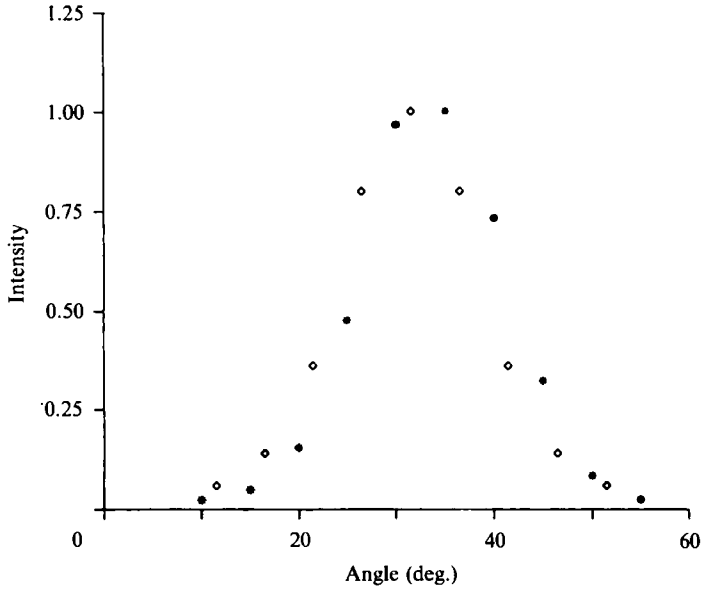

FIGURE 6. Variation of normalized average light intensity at the imager site with incident-light angle: (*a*) ✱, computed from imager data; (*b*) ◇, measured using Wolensak exposure meter.

images are formed by diffuse, rather than specular, light. There the average light intensity at the imager site, normalized by the maximum value, is shown as a function of incident angle of light for a quiescent water surface. One data set was obtained with the imager; a single frame was transferred to the VAXstation II and the average intensity among pixel sites was computed. The second data set was obtained by direct measurements of light intensity using a Wolensak exposure meter at the imager site. Both data sets yield similar results. The maximum intensity occurs for an incidence angle of about 32°, which is used in the experiments. There is a gradual reduction in light intensity as the incidence angle changes from 32°; this behaviour is characteristic of a diffuse light source. We note that light glitter, which results from light reflected directly from the water surface, may appear occasionally in an image. This glitter is easily removed (or moved) from the sampling region, prior to recording, by slight adjustments in the incidence angle of light. We also note that as wave amplitudes increase, images appear blurred in the vicinity of the wavemaker. (The origin of this blur, which is visible to the unaided eye, is not known at the present time.) The position ($x' =: x'_c, y' = 0$) of the upstream corner of the spatial sampling area (see figure 4*a*) is chosen sufficiently far downstream to circumvent this phenomenon.

Various techniques were used to compare grey levels at pixel sites with wave amplitudes and to compare the distribution of grey levels among sites with surface lengthscales. First, we imaged and analysed black and white drawings, with known wavenumber spectra. Secondly, we numerically superposed a variety of wave fields that were composed of sinusoidal wavetrains whose amplitudes and wave vectors were known. The resulting amplitudes of the wave field were assigned grey levels in the range 0–255, which corresponded to the minimum and maximum amplitudes, respectively. This image was printed on white paper, imaged, and analysed. In all of these tests, the calculated spectra faithfully reproduced the known spectra of the input patterns.

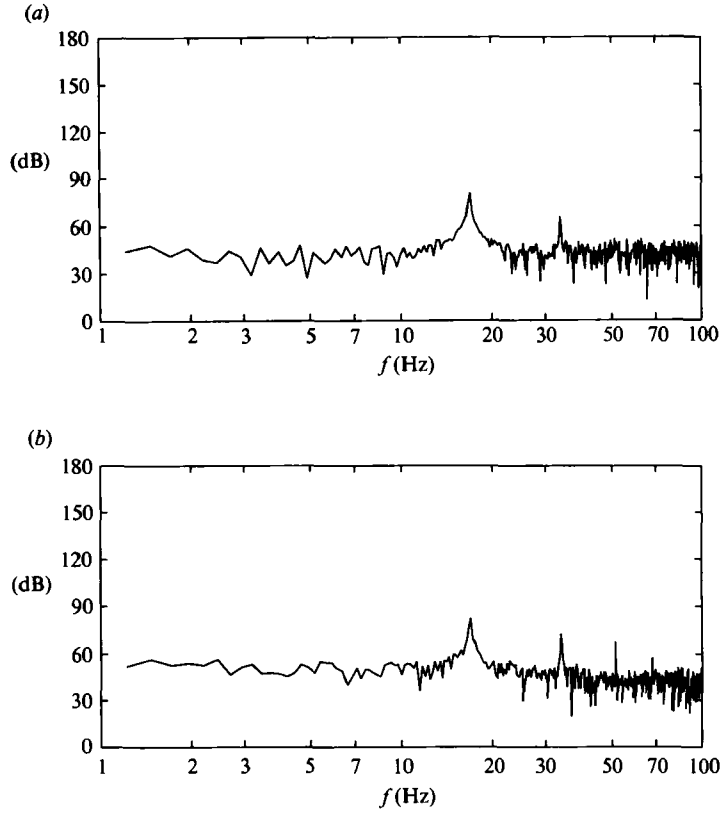

FIGURE 7. Amplitude-frequency spectra of a 17 Hz wavetrain (GC1704) calculated from time series measured simultaneously by (*a*) a wave gauge, (*b*) the imager at a nearby pixel site.

In order to compare grey levels with wave amplitudes at a pixel site, an experiment was conducted using a 17 Hz wavetrain (GC1704) and a wave gauge located in the spatial sampling region. In this experiment (only) we made simultaneous measurements with the imager and wave gauge. The imager operated at 250 f.p.s., which equalled the 250 Hz sampling rate of the continuous-time signal from the wave gauge. A digital record of 2^{10} samples from the digital signal at a pixel site, which was 0.87 cm (laterally) from the wave gauge, was compared with a corresponding record from the wave gauge. (The gauge support precluded using smaller separation distances.) Figure 7 presents the resulting amplitude-frequency spectra. The two distributions of spectral amplitudes are similar, except at higher frequencies (>50 Hz) where grey levels show the presence of third and higher harmonics of the 17 Hz wavetrain that are not present in the wave gauge signal. We suspect that these differences at high frequencies result from distortions by both measurement devices. As noted earlier, the wave gauge response is constant to 30 Hz; thereafter, signals are attenuated. Hence, the wave gauge underestimates the amplitudes of higher harmonics. Our lighting of the wavefield causes sinusoidal waves to have a square-wave appearance in the form of light and dark bands as seen in figure 4. This square-wave appearance leads to over estimates for the amplitudes of higher harmonics. In order to gain insight into the overall similarity between the wave gauge and imager measurements of wave amplitudes, we computed the linear correlation coefficient between the two digital signals; the resulting value was 0.89.

Hence, grey levels at a pixel site are reasonable measures of wave amplitudes. Herein, we are mainly interested in wavenumbers, which are obtained from the distribution of wave amplitudes within a single spatial image; hence, no effort was made in these first experiments to establish an absolute calibration between grey level and dimensional wave amplitude.

4. Presentation of experimental and theoretical results

Experimental data are presented for wavetrains with $0.29 \leqslant \tau \leqslant 2.98$, which correspond to frequencies of 8–25 Hz on clean, deep water, i.e. $T = 73$ dyn/cm and $kh \gg 1$. First, we describe the observed temporal evolution of modulationally unstable wavetrains. Secondly, we compare experimental data and theoretical predictions for wavetrains with $0.5 < \tau < 2.0$, where resonant triad interactions are not possible. Thirdly, we compare experimental data and theoretical predictions for wavetrains with $\tau > 2.0$, where resonant triad interactions are possible. Lastly, we present experimental data for Wilton $n = 2, 3$ ripples, and wavetrains with $0.155 < \tau < 0.50$.

In comparing experimental results and theoretical predictions, we note that the experiments use a water surface of finite extent, whereas the theoretical models use a water surface of infinite extent. This finite size of the experiments limits the modulational wavenumbers to countable families with minimum values $\kappa_{\min} k = 0.035$ rad/cm and $q_{\min} k = 0.103$ rad/cm in the longitudinal and transverse directions, respectively. (These values are based on the channel's length of 91 cm and breadth of 30.5 cm.)

4.1. *Temporal evolution of modulationally unstable wavetrains*

In order to show typical temporal behaviour of experimental wavetrains in the modulationally unstable band ($\tau > 0.5$), we present 131 s wave-gauge record in figure 8 from experiments GC1702 and GC1706. These records were obtained by a wave gauge at $(x', y') = (x'_c = 23, -4.7)$ cm. The 17 Hz wavetrains in these experiments had steepnesses of $\epsilon = ka_0 = 0.08$ in GC1702, which is the least nonlinear experiment, and $\epsilon = 0.31$ in GC1706, which is the most nonlinear experiment (see table 1). A comparison between the measured amplitudes in these experiments (table 3) and the viscous-threshold values (table 1) suggests that experiment GC1702 is stable and experiment GC1706 is marginally unstable. A compressed timescale is used in order to emphasize the wave envelope, rather than individual waves, and the time axes are arbitrarily shifted in order to show about 16 s of 'quiescent' water surface prior to the arrival of the wavetrain. The wave activity during this quiescent time is the ubiquitous background noise that was described in Part 2. This noise, which is mainly electrical, is broadbanded, and in experiment GC1702, its amplitude is comparable to that of the generated wavetrain. Nevertheless, the spectral analysis has no difficulty extracting the signature of the generated wavetrain. Additional wave noise is generated during an experiment by irregular contact-line motion on the wavemaker paddle and channel sidewalls. No artificial background waves are added in these experiments.

In each of the experiments shown in figure 8, a growth period of about 15 s occurred after the arrival of the wavetrain before its envelope reached a maximum, quasi-steady amplitude. This behaviour is masked somewhat in experiment GC1706 by persistent long-time variability, which we discuss below. These growth periods cannot be attributed either to wavefronts that result from speed differences between

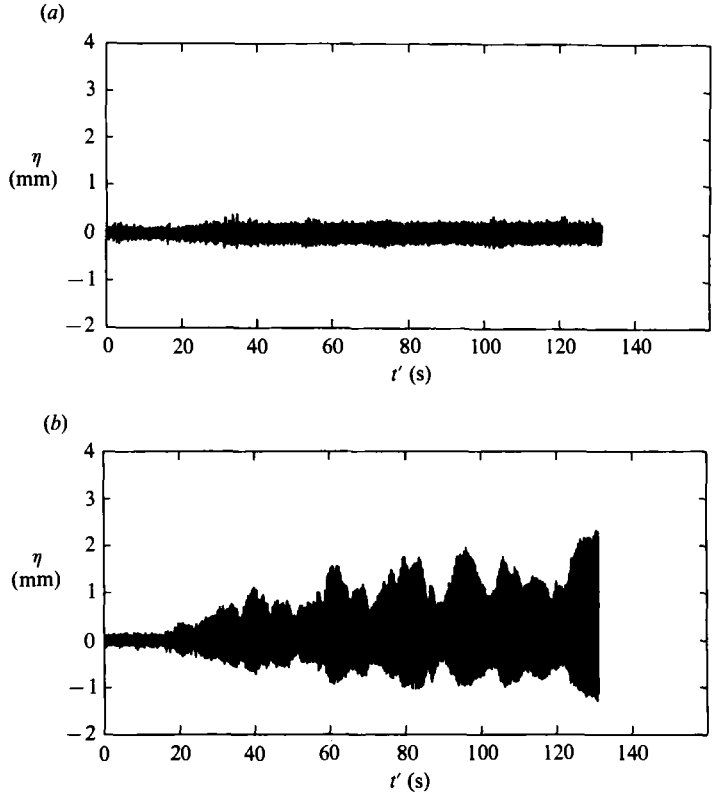

FIGURE 8. Temporal measurements by a wave gauge at $(x', y') = (x'_c = 23, -4.7)$ cm: (*a*) experiment GC1702; (*b*) experiment GC1706.

wave energy and wave phase or to transient waves generated during the start-up of the wavemaker. (The minimum energy speed among all wavetrains is $U = 17.8$ cm/s, which occurs for $f = 6.4$ Hz ($\tau = 0.155$), and the minimum phase speed is 23.2 cm/s, which occurs for $f = 13.6$ Hz ($\tau = 1$).) We believe they are related to multiple reflections of the generated wavetrain at the end of the 91 cm channel, which opens into the larger basin. (Experiments with shorter channel lengths were inconclusive.) If so, the wavefield in the channel contains some standing waves, which are masked by the unstable behaviour of the progressing wavetrain.

Even after the initial growth period in experiment GC1706 of figure 8(*b*), considerable envelope variability persists that cannot be attributed to naturally occurring background waves – amplitude changes by a factor of two are observed. These large-amplitude modulational cycles generally occur over hundreds of wave periods, which is much longer than our third-order NLS equations are expected to remain applicable. There is some variability on the shorter timescale that is appropriate to NLS equations, i.e. $t' \sim 2\pi/\omega\epsilon^2 \approx 1s$; however, most of this variability is within the background noise level. Since this long-time variability increases with increasing steepness of the wavetrain, we believe that it results from weaker nonlinear interactions, such as (non-degenerate) resonant quartets, resonant quintets, etc., and resonant triads when $\tau > 2.0$.

Observations of the water surface indicate that the persistent long-time unsteadiness in figure 8(*b*) is manifest by to-and-fro meandering of striations, i.e. of envelope nodal lines (see §2.2.2 and Part 1). The effect of this meandering pattern on

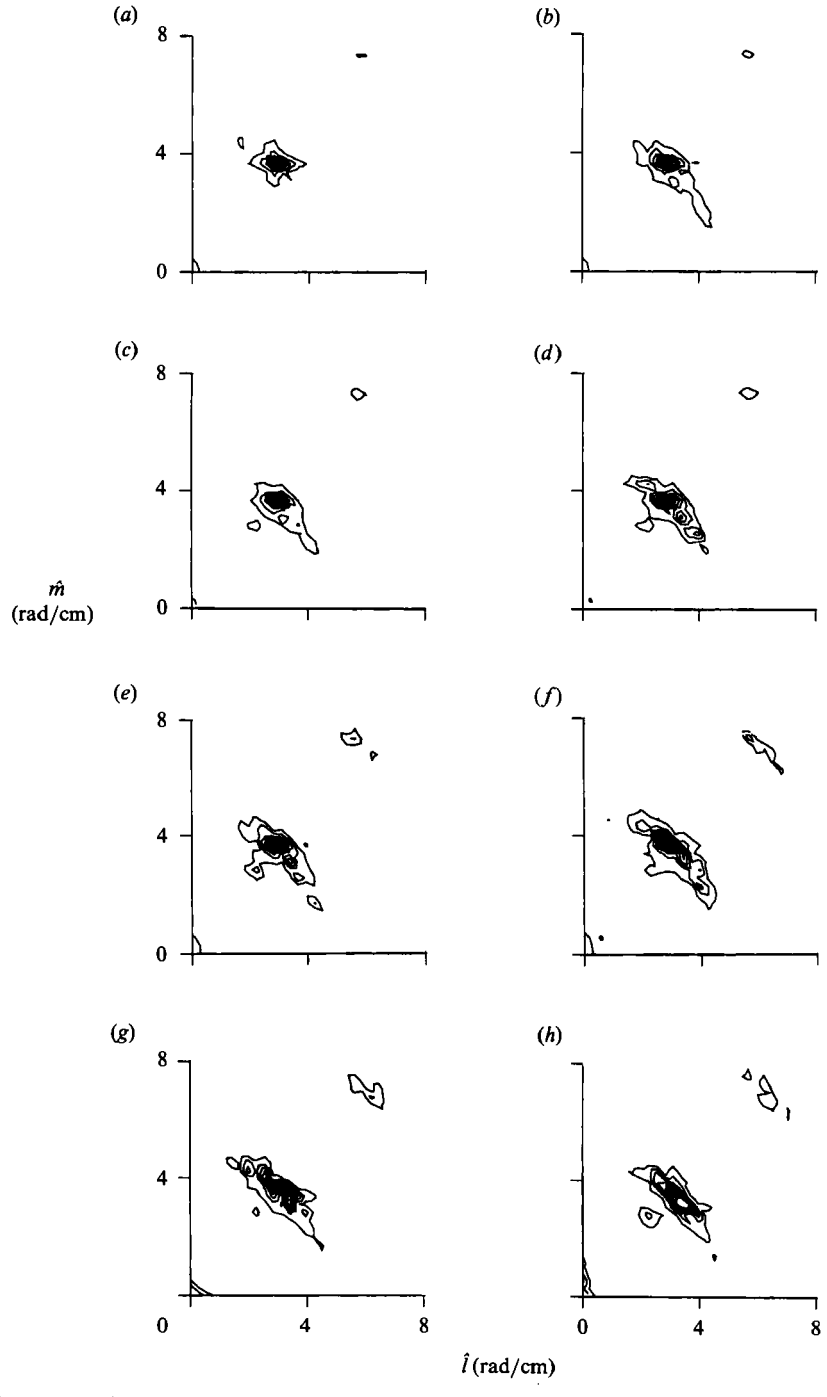

FIGURE 9. Temporal evolution of two-dimensional wavenumber spectra for experiment GC1706. Spectra are at a time, $\Delta t'$, after the wavetrain reached the spatial sampling region, and contain ten amplitude contours at equally spaced intervals to their maximum spectral amplitude, $\mathscr{A}$ (in arbitrary units): (*a*) $\Delta t' \approx 10$ s, $\mathscr{A} = 19.1$; (*b*) $\Delta t' \approx 20$ s, $\mathscr{A} = 23.4$; (*c*) $\Delta t' \approx 30$ s, $\mathscr{A} = 29.9$; (*d*) $\Delta t' \approx 40$ s, $\mathscr{A} = 27.6$; (*e*) $\Delta t' \approx 50$ s, $\mathscr{A} = 27.6$; (*f*) $\Delta t' \approx 60$ s, $\mathscr{A} = 23.4$; (*g*) $\Delta t' \approx 80$ s, $\mathscr{A} = 24.5$; (*h*) $\Delta t' \approx 110$ s, $\mathscr{A} = 23.8$.

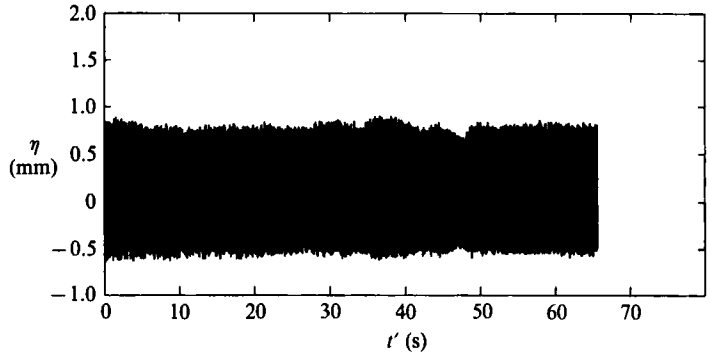

FIGURE 10. Temporal wave measurements by a wave gauge at $(x', y') = (5.0, -4.7)$ cm for experiment GC1706.

Experiment	f (Hz)	s (mm)	x_c' (cm)	a_0† (cm)	ka_0
GC2502	25	0.20	23	0.018	0.114
GC2503	25	0.30	23	0.028	0.176
GC2504	25	0.40	23	0.027	0.171
GC1702	17	0.20	23	0.017	0.078
GC1704	17	0.40	23	0.048	0.219
GC1706	17	0.60	23	0.068	0.311
GC1305	13.6	0.50	37	0.047	0.174
GC1306	13.6	0.60	37	0.059	0.216
GC9802	9.8	0.20	23	0.015	0.039
GC9810	9.8	1.00	23	0.096	0.249
GC0806	8.0	0.60	23	0.058	0.116

†a_0 was measured at $(x', y') = (5, -4.7)$ cm.

TABLE 2. Experimental parameters. $h = 4.92$ cm, $T = 73$ dyn/cm, $b = 30.5$ cm.

spatial measurements is shown in figure 9 by a sequence of measured, two-dimensional, wavenumber spectra that were obtained during experiment GC1706 at various times ($\Delta t'$) after the wavetrain reached the spatial sampling region. Each spectrum is shown in the rotated wave-vector space, i.e. $\hat{\boldsymbol{k}} = (\hat{l}, \hat{m})$, with ten amplitude contours up to the maximum spectral amplitude, which is listed in arbitrary units. The first spectrum of figure 9(*a*) ($\Delta t' \approx 10$ s) shows a spike that corresponds to the 17 Hz wavetrain. There is evidence of the hypocycloid shape, which is not physical (see §3.2), second-harmonic generation, which is probably physical (see §3.3), and slight amplification of oblique waves in a transverse modulational band, which is physical. The second spectrum of figure 9(*b*) ($\Delta t' \approx 20$ s) shows continued amplification of the 17 Hz wavetrain, its second harmonic, and oblique waves in the transverse modulational band; the hypocycloid shape has disappeared. The third spectrum of figure 9(*c*) ($\Delta t' \approx 30$ s) shows the first amplification of collinear waves with a lower wavenumber magnitude than that of the 17 Hz wavetrain. The fourth spectrum of figure 9(*d*) ($\Delta t' \approx 40$ s) shows the continued amplification of oblique waves in the transverse modulational band, the emergence of dominant transverse wavenumbers, and the continued amplification of collinear waves in the longitudinal modulational band. This spectrum is representative of the quasi-steady conditions in the subsequent spectra. Oblique wavetrains in the transverse modulational band persist; in fact, their amplitudes

become sufficiently large to generate second harmonics, e.g. see figure 9(*f*). Collinear wavetrains in longitudinal modulational bands are less persistent; in fact, most exhibit growth-decay cycles, although one dominant wavetrain is always present. The spectral amplitude of the 17 Hz wavetrain varies about 10% during this quasi-steady evolution. We note that these spatial data take longer than temporal data to reach the quasi-steady condition; this result is explained subsequently.

The initial growth periods, the long-time variability of envelope amplitudes in our more nonlinear experiments, and viscous damping make it difficult to obtain the wavetrain amplitude a_0 from downstream measurements. In order to circumvent this difficulty, we routinely made 65 s time-series measurements upstream at $(x', y') = (5, -4.7)$ cm. These measurements, which were recorded after the initial growth periods, were nearly uniform in amplitude, as illustrated in figure 10 for experiment GC1706. The average amplitude from each of these records was measured; results are listed in table 2, which also shows other measurements from our experiments.

4.2. *Experimental and theoretical results for wavetrains with* $\tau > 0.5$

The inviscid, uncoupled NLS equations (14) and (21) indicate that ripple wavetrains with $\tau > 0.5$ are unstable to both longitudinal and transverse modulations, and that both modulations should amplify at about the same spatial rate. Here we compare experimental results with the theoretical predictions of these equations that are summarized in table 3. In this comparison we also account for the effects of weak viscosity that are summarized in table 1.

4.2.1. *Wavetrains with* $0.5 < \tau < 2.0$

For ripple wavetrains with $0.5 < \tau < 2.0$, which correspond to $9.8 < f < 19.6$ Hz, resonant quartet interactions can occur but resonant triads cannot (see Parts 1 and 2); hence, these wavetrains are most appropriate for comparison with predictions of the NLS equations.

Figure 11 shows temporal data from three experiments with 17 Hz wavetrains whose initial amplitudes were varied. The wave-gauge time series in column (*d*), which were recorded at $(x', y') = (x'_c, -4.7$ cm), show that the long-time variability of the envelope amplitude increases with the wavetrain's amplitude. The frequency spectra in column (*e*) show a corresponding increase in the number and amplitudes of superharmonic wavetrains. The frequency spectra indicate that wavetrains with modulational frequencies did not amplify in these experiments; no significant growth of frequency sidebands is evident in either spectrum. The absence of sideband instabilities in the frequency spectra is not surprising in experiments GC1702 and GC1704, since the amplitudes of both wavetrains were below the viscous-threshold values. However, modulational instabilities did occur in experiment GC1706 as shown in figure 9; hence, it is surprising that no sideband growth occurred in its frequency spectrum. In fact, modulational instabilities also occurred in experiment GC1704, as we now show.

Figure 12 shows experimental and inviscid, theoretical spatial data in rows (*a*)–(*c*) for the three 17 Hz experiments of figure 11. Column (*d*) shows water-surface images; column (*e*) shows the corresponding two-dimensional wavenumber spectra; and column (*f*) shows the theoretical predictions that include the bands of unstable transverse ($-Qk \leqslant q \leqslant Qk$) and longitudinal ($-Kk \leqslant \kappa \leqslant Kk$) wavenumbers, the most unstable wavenumbers $\pm q_m k$ and $\pm \kappa_m k$, and quarter of a circle that represents the isotropic dispersion relation (1), with $k^2 = \hat{l}^2 + \hat{m}^2$, for a 17 Hz wavetrain. The wavenumber spectra in column (*e*) are normalized by the spectral

	BF longitudinal instability						BF transverse instability					
$\lvert A_0\rvert$ (measured)	$\pm\kappa_m$	$\pm\kappa_m k$ (rad/cm)	Λ_x (cm)	$\pm Kk$ (rad/cm)	$10^3\gamma_m$	e_x (cm)	$\pm q_m$	$\pm q_m k$ (rad/cm)	Λ_y (cm)	$\pm Qk$ (rad/cm)	$10^3\Gamma_m$	e_y (cm
0.062	0.062	0.283	22.0	0.403	1.86	209	0.043	0.196	32.3	0.275	0.91	241
0.175	0.176	0.803	7.8	1.139	14.82	26	0.121	0.552	11.4	0.778	7.25	30
0.248	0.250	1.141	5.5	1.613	29.73	13	0.171	0.780	8.1	1.101	14.56	15
0.123	0.209	0.772	8.2	1.090	15.57	25	0.141	0.521	12.0	0.739	10.00	27
0.155	0.262	0.968	6.5	1.368	24.54	16	0.178	0.658	9.6	0.927	15.75	17
0.114	0.065	0.411	15.3	0.579	2.87	137	0.043	0.272	22.9	0.389	0.95	167
0.177	0.101	0.639	9.9	0.901	6.95	57	0.068	0.430	14.7	0.605	2.29	69
0.170	0.097	0.614	10.2	0.869	6.46	61	0.065	0.411	15.2	0.583	2.13	74

ummary of (inviscid) theoretical results for unstable transverse and longitudinal modulations, based on measured wavetrai

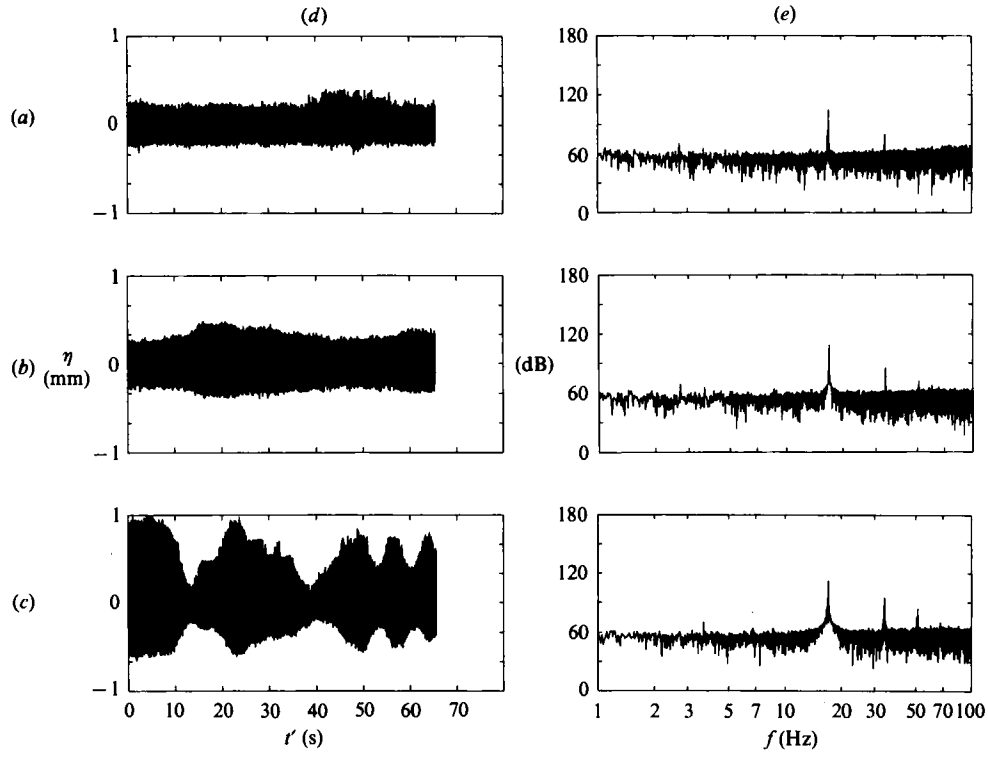

FIGURE 11. Temporal data for experiments with 17 Hz wavetrains: $(x', y') = (5.0, -4.7)$ cm. Row (a) experiment GC1702; row (b) experiment GC1704; row (c) experiment GC1706; column (d) wave-gauge measurements; column (e) amplitude-frequency spectra.

amplitude of the 17 Hz wavetrain with the largest spectral amplitude (GC1704); hence, the contour interval is the same for each spectrum. The theoretical bands of unstable wavenumbers in column (f) are centred about the theoretical location of a 17 Hz wavetrain, which is directed at the observed angle in the experiment; a band thickness of 0.284 rad/cm, which corresponds to our measurement resolution, is used.

In the least nonlinear experiment (GC1702, $\epsilon = 0.078$) of figure 12, row (a), the water-surface image shows a one-dimensional wave pattern. Spectral amplitudes for this image are concentrated in a small region of wavenumbers that corresponds to the 17 Hz wavetrain; the region has dimensions that are comparable to our wavenumber resolution. (Note the similarity between this spectrum and that of figure 5(b) for an analytical sine wave.) Neither collinear nor transverse wavetrains with modulational wavenumbers have amplified, as expected, since the wavetrain's amplitude is substantially below the viscous-threshold values.

In the more nonlinear experiment (GC1704, $\epsilon = 0.219$) of figure 12, row (b), the water-surface image shows a wave pattern that is weakly two-dimensional; slight 'kinks' occur in wave crests. Spectral amplitudes for this image are concentrated in wavenumber regions that correspond to the 17 Hz wavetrain, its second-harmonic, and oblique wavetrains with modulational wavenumbers in a transverse band about the 17 Hz wavetrain. (The vertical elongation of amplitude contours is an artifact of the numerical algorithm, see §3.2.) The measured bandwidth agrees well with the predicted (inviscid) bandwidth Qk, and a dominant oblique wavetrain is emerging whose modulational wavenumber agrees well with the predicted $-q_m k$. The

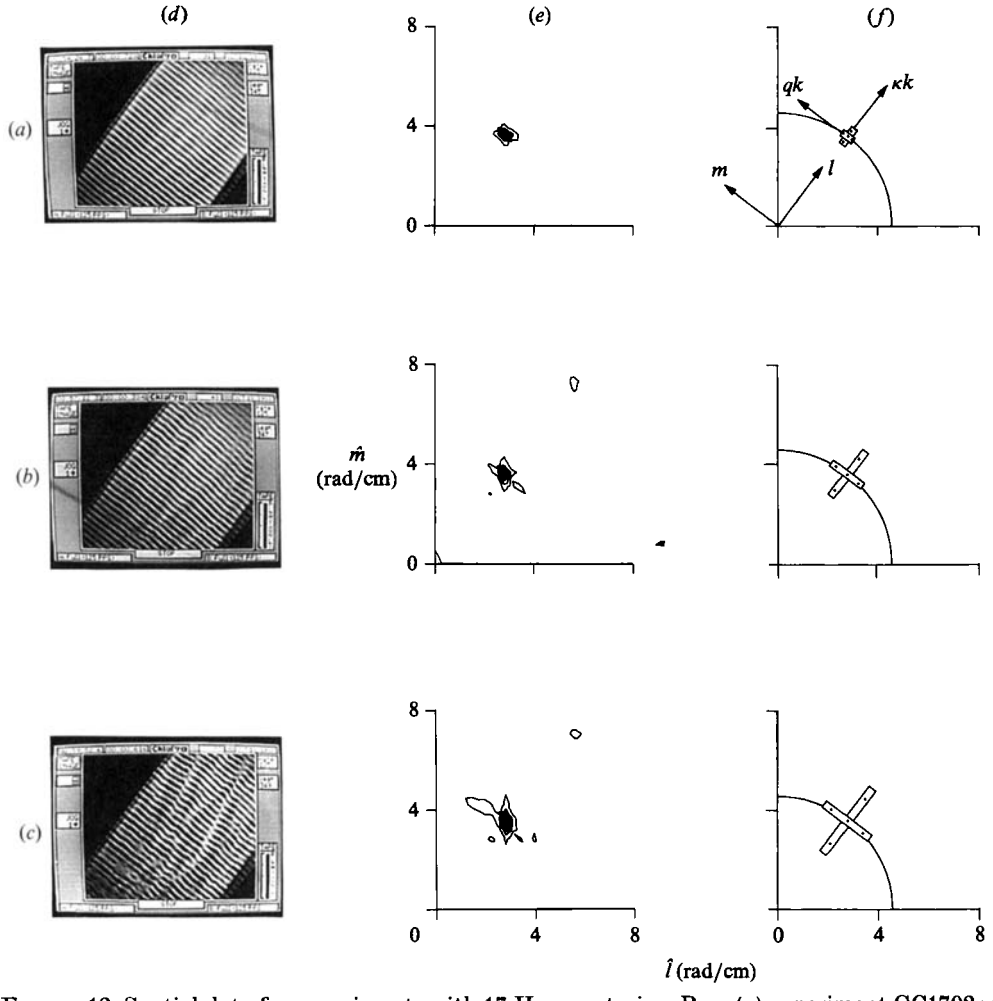

FIGURE 12. Spatial data for experiments with 17 Hz wavetrains. Row (*a*) experiment GC1702; row (*b*) experiment GC1704; row (*c*) experiment GC1706; column (*d*) water surface images; column (*e*) measured two-dimensional wavenumber spectra; column (*f*) predicted (inviscid) bands of unstable waves (large cross-shapes), and ——, the dispersion relation, for a 17 Hz wavetrain.

measured spectrum shows the amplification of one collinear wavetrain whose modulational wavenumber is slightly larger than the predicted $-\kappa_m k$. The *e*-folding distances for both modulational instabilities are comparable to the distance to the spatial sampling region, and to the *e*-folding distance for viscous damping. Note that these modulational instabilities have occurred even though the wavetrain's amplitude is below the viscous-threshold values.

In the most nonlinear experiment (GC1706, $\epsilon = 0.311$) of figure 12, row (*c*), the wave pattern is two-dimensional; striations criss-cross the channel; and the alternating light and dark bands across a striation indicate that 180° phase jumps occurred. (The amplitude of this wavetrain is about equal to the viscous-threshold values.) Spectral amplitudes for this image are concentrated in wavenumber regions that correspond to the 17 Hz wavetrain, its second-harmonic, and oblique wavetrains with modulational wavenumbers in a transverse band about the 17 Hz wavetrain. There is asymmetry in the development of the transverse band; most amplification

occurred for modulations with $q > 0$. However, symmetric ($\pm q$) development was observed in other experiments, e.g. see figure 11, so this asymmetry is probably inconsequential. (Whether wavetrains with $+q$ or $-q$ modulations amplify depends on the naturally occurring background waves, which differ between experiments, and on the channel sidewalls, which eventually enforce symmetry in the spectrum through reflections.) The measured transverse bandwidth exceeds the predicted (inviscid) $+Qk$, and it forms an arc that is coincident with the dispersion-relation circle for the 17 Hz wavetrain. There is no experimental evidence that the predicted most-unstable transverse modulation, $q_m k = 0.780$, was dominant; hence, we should not expect striations in the wave pattern to be parallel to the channel axis. In fact, many of the striations have angles of $\theta_s \approx 12°$, which, according to (30), corresponds to a transverse wavenumber of $q_s k \approx 0.275$ rad/cm and wavelength of 22.9 cm. The amplification of collinear wavetrains remains weak and concentrated in a dominant wavenumber that is less than the predicted $-\kappa_m k$. We note that longitudinal modulations did develop more fully in other GC1706 experiments as shown in figure 11, but they were always confined to $\kappa < 0$. This asymmetry might be consequential, since it is consistent with experimental results for BF instabilities of gravity wavetrains (e.g. see Lake *et al.* 1977) in which the lower frequency, most unstable wavetrain dominates during long-time evolution.

In summary, the wavenumber spectra shows that 17 Hz wavetrains are most unstable to oblique wavetrains, and that these instabilities occur even when the wavetrain's amplitude is below the viscous-threshold values. The frequency spectra indicate that the amplified, oblique wavetrains have the same frequency as the underlying wavetrain; hence, the dominant instability in these experiments is a rhombus-quartet.

Figure 13 shows experimental and theoretical results for experiment GC1305 in row (*a*) and experiment GC1306 in row (*b*); both experiments used 13.6 Hz wavetrains ($\tau = 1$) whose amplitudes were about equal to the viscous-threshold values. The frequency spectra in column (*c*) show amplitude spikes at 13.6 Hz and its superharmonics, but do not show amplification of wavetrains with modulational frequencies. Nevertheless, the spatial data in column (*d*) indicate pronounced amplification of wavetrains with transverse modulational wavenumbers; the measured bandwidths exceed inviscid predictions, which are shown in column (*e*). These bands also form arcs that coincide with the dispersion-relation circle for the 13.6 Hz wavetrains. There is no indication that the predicted most-unstable transverse modulations were dominating in these experiments. Striations in the wave pattern of experiment GC1306 (not shown) have an angle of about 16°, which corresponds to a transverse wavenumber of $q_s k \approx 0.193$ rad/cm and wavelength of 32.6 cm. No amplification of collinear wavetrains in longitudinal modulational bands has occurred in either experiment.

4.2.2. *Wavetrains with* $\tau > 2.0$

Resonant triad interactions are possible for ripple wavetrains with $\tau > 2.0$, which corresponds to $f > 19.6$ Hz on clean, deep water. Parts 1 and 2 of this series examined resonant triad interactions in detail. In Part 2, it was shown that specific triad(s) were selectively amplified from the continuum of possible triads when the background wave spectrum contained discrete components(s). It was also shown that all wavetrains in the continuum of possible triads were amplified when the background wave spectrum was broadbanded, as it is herein. Moreover, transverse modulational instabilities were crucial to both resonant-triad behaviours.

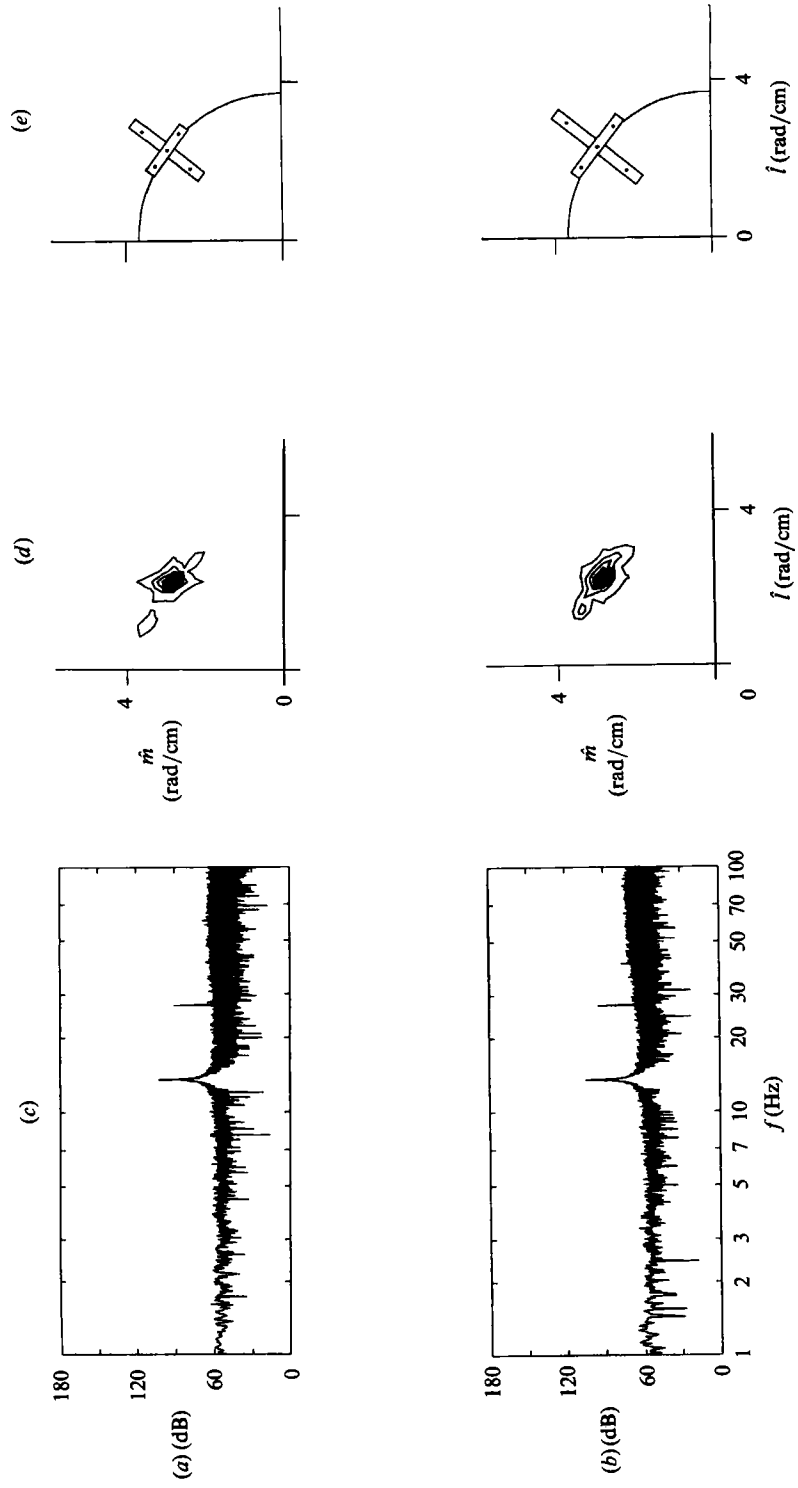

FIGURE 13. Measured and theoretical results for experiments with 13.6 Hz wavetrains. Row (*a*) experiment GC1305; row (*b*) experiment GC1306; column (*c*) amplitude-frequency spectra; column (*d*) measured wave-vector spectra; column (*e*) predicted (inviscid) bands of unstable waves (large cross-shapes), and ——, the dispersion relation, for a 13.6 Hz wavetrain.

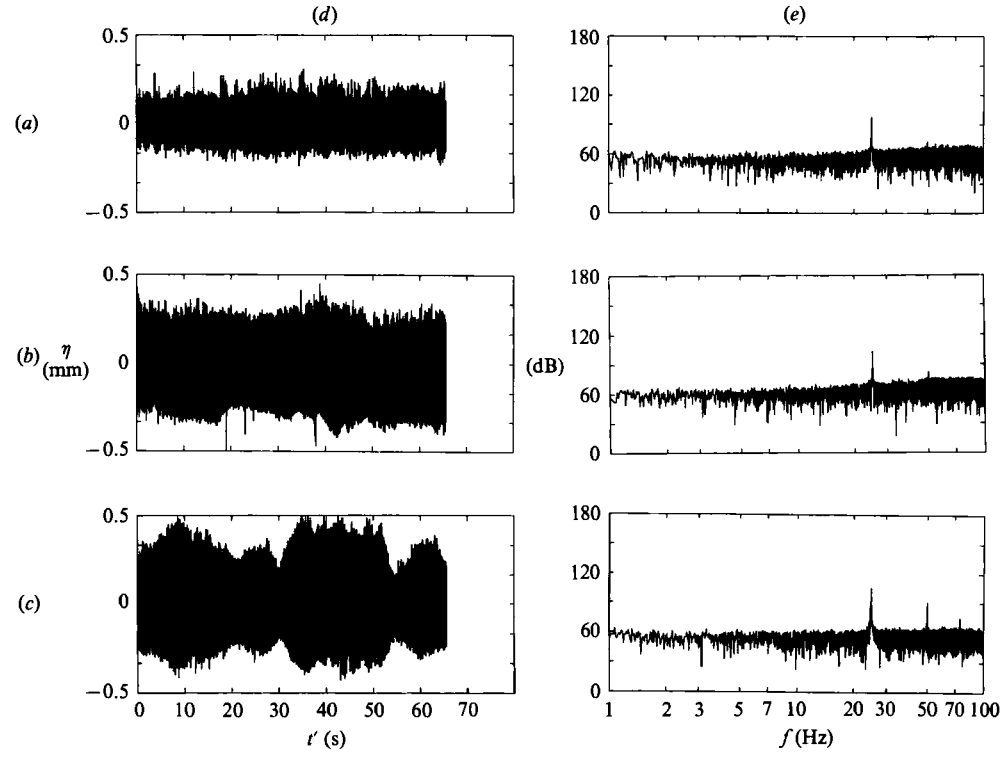

FIGURE 14. Temporal data for experiments with 25 Hz wavetrains. Row (*a*) experiment GC2502; row (*b*) experiment GC2503; row (*c*) experiment GC2506; column (*d*) wave-gauge measurements; column (*e*) amplitude-frequency spectra.

Figure 14 shows temporal data from three experiments with 25 Hz wavetrains whose initial amplitudes were varied; note that all of these amplitudes were significantly smaller than the viscous-threshold values. The data in figure 14 show that the long-time variability of the envelope amplitude increases with the wavetrain's amplitude. However, there is more short-time variability than in figure 11 for the 17 Hz wavetrain, presumably in consequence of resonant triad interactions. The corresponding frequency spectra show that the number and amplitudes of superharmonics increase with the wavetrain's amplitude. No wavetrains with modulational frequencies have amplified; however, oblique wavetrains with the same frequency as the underlying wavetrain have amplified, as shown in figure 15.

Figure 15 shows experimental and inviscid, theoretical spatial data in rows (*a*)–(*c*) for the three 25 Hz experiments of figure 14. In the smallest-amplitude experiment, GC2502 of row (*a*), the wave pattern is nearly one-dimensional, and, according to the measured wavenumber spectrum, neither collinear nor oblique wavetrains have amplified. (The vertical elongation of amplitude contours is an artifact of the numerical algorithm, see §3.2 and figure 5*c*.) This behaviour is consistent with viscous predictions, i.e. the predicted, inviscid bandwidths for modulational instabilities shown in figure 15 row (*a*) vanish.

Wavetrain amplitudes increase in experiments GC2503 and GC2504, which are shown in figure 15, rows (*b*) and (*c*), respectively, but remain significantly smaller than the viscous-threshold values. The amplitude in experiment GC2504 is slightly lower than in experiment GC2506, even though the wavemaker stroke is slightly

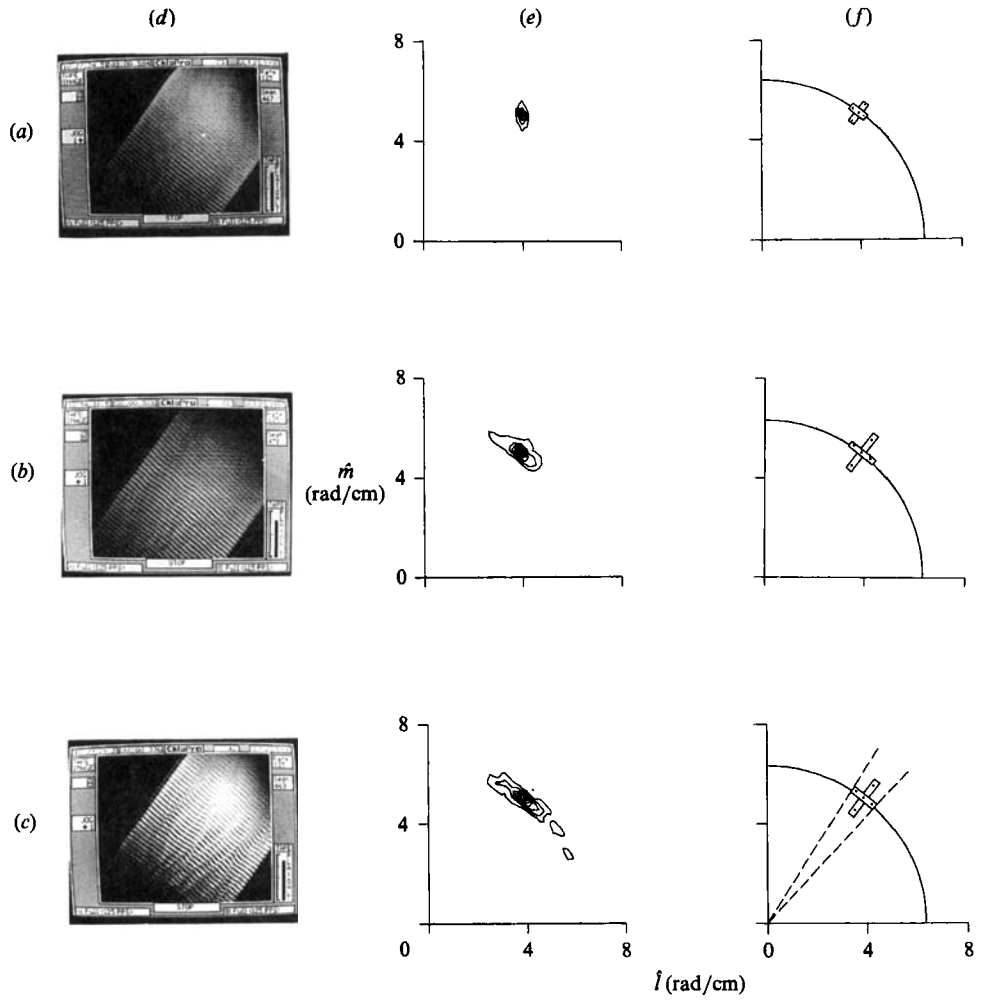

FIGURE 15. Spatial data for experiments with 25 Hz wavetrains. Row (*a*) experiment GC2502; row (*b*) experiment GC2503; row (*c*) experiment GC2504; column (*d*) water surface images; column (*e*) measured two-dimensional wavenumber spectra; column (*f*) predicted (inviscid) bands of unstable waves (large cross-shapes), and ——, the dispersion relation, for a 25 Hz wavetrain.

larger. This behaviour was also observed in Part 1, where it was conjectured that more energetic transfer of the wavetain's energy to other wavetrains by resonant interactions might be responsible. The wave patterns shown in column (*d*) are two-dimensional; some striations are wide and parallel to the channel axis, and no phase jumps occur across them. The measured wavenumber spectra in column (*e*) show pronounced amplification of oblique wavetrains in a band of transverse modulational wavenumbers. The measured bandwidth in experiment GC2504 greatly exceeds that in experiment GC2503 as well as the inviscid prediction, which is shown in column (*e*). Wave energy has spread to a directional half-angle of 22°, rather than the (inviscid) prediction of 5.3°, which is shown in column (*f*). (Note that the 22° angle is based on the first contour level; hence, this angle would increase if we used more contours.) The measured spectrum in experiment GC2503 shows amplification of only one collinear wavetrain whose modulational wavenumber is nearly twice the predicted $-\kappa_m k$. The measured spectrum in experiment GC2504 is unique among

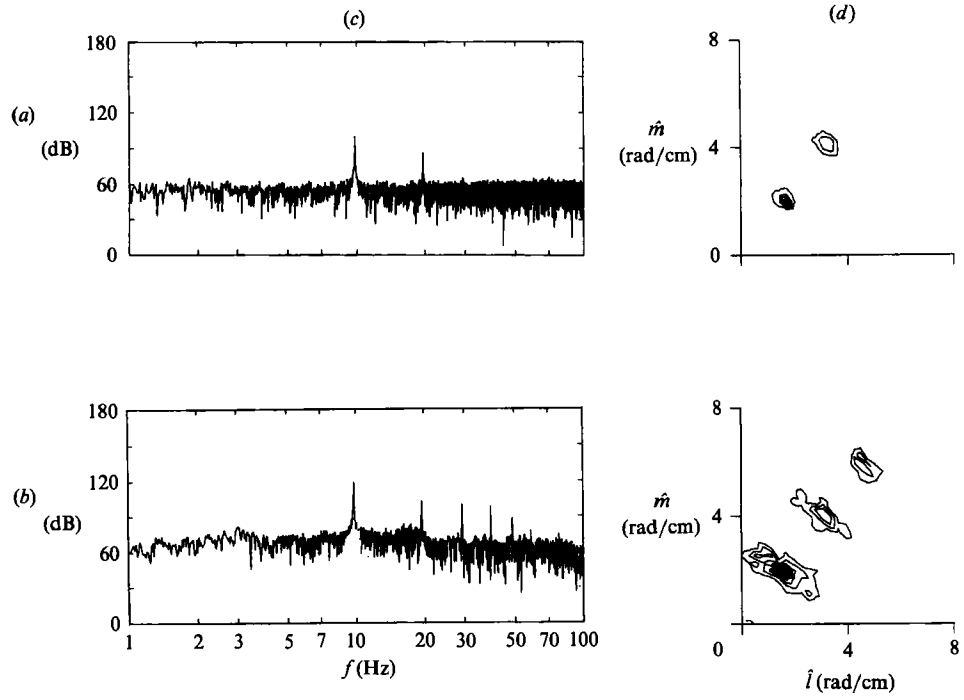

FIGURE 16. Measured data for experiments with 9.8 Hz wavetrains. Row (*a*) experiment GC9802; row (*b*) experiment GC9810; column (*c*) amplitude-frequency spectra; column (*d*) wave-vector spectra.

our experiments; it shows amplification of a collinear wavetrain in the $\kappa > 0$ portion of the longitudinal modulational band. The measured wavenumber is slightly less than the predicted $+\kappa_m k$.

4.3. *Experimental results for wavetrains with* $0.155 < \tau \leqslant 0.5$

Wavetrains with $0.155 < \tau < 0.5$, which correspond to $6.4 < f < 9.8$ Hz, are stable to both longitudinal and transverse modulations, according to our uncoupled, third-order NLS equations. (In addition, Hogan (1985) showed that longitudinal modulations remain stable at fourth-order.) At $f = 9.8$ Hz (Wilton $n = 2$ ripples) the NLS equations are no longer applicable owing to a singularity in one of their coefficients. In addition, four higher-order Wilton ripples are embedded within this frequency range; their frequencies are: $n = 3, f = 8.4$ Hz; $n = 4, f = 7.5$ Hz; $n = 5$, $f = 7.0$ Hz, and $n = 6, f = 6.6$ Hz. McGoldrick (1972) conducted experiments in the neighbourhoods of these frequencies, and found that all of these internal resonances were easily excited, even when detuned significantly from the theoretically resonant frequency. Here, we present experimental results (only) for $6.4 < f \leqslant 9.8$ Hz.

4.3.1. *Wilton* $n = 2$ *ripples*

Figure 16 shows measured frequency and wavenumber spectra for two experiments with 9.8 Hz wavetrains whose initial amplitudes were varied. The wave steepness in experiment GC9802 is very small ($\epsilon = 0.039$); nevertheless, both the frequency and wavenumber spectra in row (*a*) of figure 16 show significant amplitudes for the 19.6 Hz superharmonic wavetrain. There is no evidence that either oblique or collinear wavetrains have amplified.

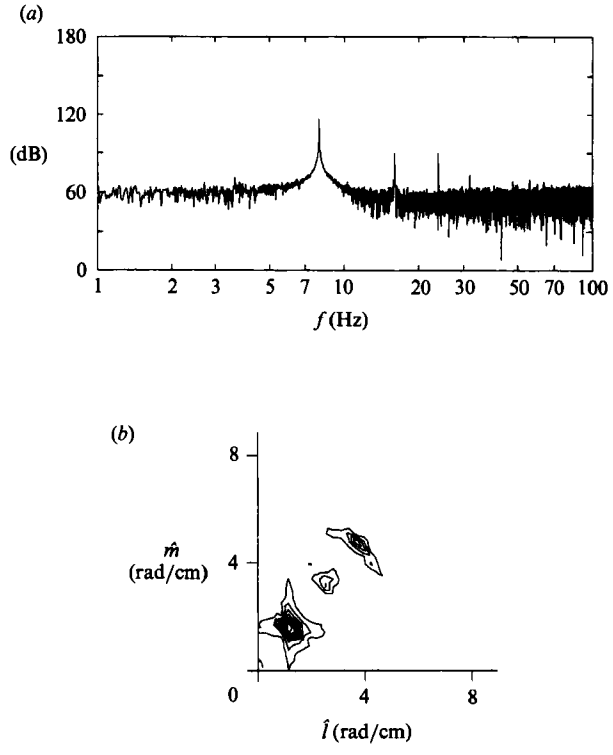

FIGURE 17. Measured data for experiment GC0806 with an 8.0 Hz wavetrain: (*a*) amplitude-frequency spectrum; (*b*) wave-vector spectrum.

When the wave steepness is increased to $\epsilon = 0.249$ in experiment GC9810 of figure 16, row (*b*), superharmonics of the 9.8 Hz wavetrain proliferate; five superharmonics appear in the frequency spectrum and two superharmonics appear in the wavenumber spectrum. In addition, there is energetic amplification of oblique wavetrains in bands of transverse modulational wavenumbers for both the 9.8 and 19.6 Hz wavetrains. There is no experimental evidence that collinear wavetrains with longitudinal modulational bands have amplified. Hence, the 9.8 Hz is unstable to oblique wavetrains in a band of transverse modulational wavenumbers, and after the second-harmonic wavetrain is amplified by internal resonance, it also becomes unstable to oblique wavetrains.

4.3.2. *The 8 Hz wavetrain and Wilton $n = 3$ ripples*

In order to examine the modulational stability of wavetrains with $6.4 < f < 9.8$ Hz, we conducted experiments using 8 Hz wavetrains. McGoldrick's (1972) experiments found that third-harmonic resonance was excited down to 8.06 Hz while fourth-harmonic resonance was excited up to 7.94 Hz. Hence, 8 Hz is in the middle of a frequency range where wavetrain evolution might not be dominated by internal resonance – this was not the case.

Figure 17 presents frequency and wavenumber spectra for experiment GC0806. Even though the wave steepness is fairly small ($\epsilon = 0.116$), the frequency spectrum in figure 16(*a*) shows several superharmonics, and the spectral amplitude of the third-harmonic (24 Hz) is larger than that of the second (16 Hz); hence, third-harmonic resonance has occurred. (We note that on clean, deep water, third-

harmonic resonance occurs when $f = 8.37$ Hz according to the inviscid, and $f = 8.39$ Hz according to the viscous, dispersion relation.) The wavenumber spectrum in figure 17(*b*) shows further evidence of third-harmonic resonance. (The water-surface image used to obtain this wavenumber spectrum is shown in figure 4*b*.) Amplitude contours that are centred about wavenumbers for the 8 Hz wavetrain show the hypocycloid shape, which is not physical (see §3.2); there is no evidence of modulational instabilities. Amplitude contours that are centred about wavenumbers for the 16 Hz second harmonic are localized and nearly circular. Amplitude contours that are centred about wavenumbers for the 24 Hz third harmonic form a narrow, transverse band that bends in an arc that is coincident with the dispersion circle for a 24 Hz wavetrain. No collinear wavetrains have amplified for either the 8 Hz or 24 Hz wavetrains.

5. Discussion and conclusions

All of our experiments show that ripple wavetrains with $\tau \geqslant 0.5$ ($f \geqslant 9.8$ Hz) and sensible amplitudes ($\epsilon > 0.15$) are unstable to transverse and longitudinal modulations, i.e. resonant quartets of the Benjamin–Feir type. In addition, the experiments show that amplification of transverse modulations dominates amplification of longitudinal modulations. The absence of amplification of wavetrains with modulational frequencies in frequency spectra and the presence of amplification of oblique wavetrains with transverse modulational bands in two-dimensional wavenumber spectra indicate that ripple wavetrains are most unstable to oblique wavetrains with the same frequency, i.e. a rhombus-quartet instability, similar to the conjecture of Henderson (1986). This result is consistent with our observation that wave-vector spectra require longer than frequency spectra to become quasi-steady. Further evidence of the dominance of rhombus-quartet instability is seen in experimental wave-vector spectra where the transverse bands of amplified waves form arcs that are coincident with the dispersion-relation circle of the underlying wavetrain. The rhombus-quartet instability, which is the most-degenerate resonant quartet possible, remains dominant for wavetrains with $\tau > 2$, where resonant triad interactions occur – if the phenomenon of selective amplification does not occur (see Parts 1 and 2); even then, the rhombus-quartet instability plays a crucial role. These rhombus-quartet instabilities are robust; they occur for wavetrains with amplitudes significantly below the expected viscous-threshold values, and their bandwidths sometimes exceed the inviscid predictions.

Collinear wavetrains with longitudinal modulational wavenumbers also amplified in the experiments with $\tau > 0.5$, but more slowly than oblique wavetrains, and they were less persistent. Their amplification was more consistent with predictions that included the effects of viscosity. The apparent absence of modulational frequencies corresponding to these modulational wavenumbers is also indicative of the weakness of longitudinal instabilities, relative to the transverse modulations. Most of the collinear wavetrains that amplified appeared to undergo growth-decay cycles. In all but one experiment, amplification of collinear wavetrains was confined to negative modulational wavenumbers; hence, the wave-vectors of the amplified waves have smaller magnitudes than that of the underlying wavetrain. This behaviour is consistent with the dominance of the lower sideband frequency observed in the evolution of gravity wavetrains.

The occurrence of longitudinal and transverse modulational instabilities for ripple wavetrains with $\tau > 0.5$ is predicted by uncoupled NLS equations (14) and (21),

respectively; however, these equations do not predict the dominance of rhombus-quartet instabilities. In addition, the inviscid NLS equation for the transverse instability typically underpredicts the measured bandwidth of unstable wavenumbers. The inviscid NLS equation for the longitudinal instability typically overpredicts the bandwidth of unstable wavenumbers, as expected when the inviscid results are modified to account for viscosity. Nevertheless, there is often good agreement between the predicted and measured most unstable (negative) longitudinal wavenumber.

The observed dominance of instabilities by oblique perturbations during the evolution of ripple wavetrains with $\tau > 0.5$ is qualitatively consistent with numerical results of Chen & Saffman (1985, e.g. their figure 3) for capillary wavetrains with moderate amplitudes. However, their results for BF (class I) and quintet (class II) instabilities of capillary waves do not suggest the dominance of rhombus quartets.

The numerical results of Zhang & Melville (1987, their figure 4*b*) include one case in which the underlying ripple wavetrain has $\tau = 3.0$ and $\epsilon = 0.15$, which are nearly equal to the parameters for experiments GC2503 and GC2504. Surprisingly, their results indicate that BF instabilities disappear for small transverse and longitudinal wavenumbers (whose dimensional values are smaller than our measurement resolution). BF instabilities do exist in a region of larger transverse and longitudinal wavenumbers, but there is no indication in their results that transverse modulations are dominant.

Our experimental results for $\tau > 0.5$ do not provide evidence of bifurcations of ripple wavetrains; however, the steepnesses of the experimental wavetrains were probably too small to expect bifurcations. (Zhang & Melville (1987) found a threshold steepness of $\epsilon = 0.39$ when $\tau = 3.0$ in order to obtain a neutrally stable perturbation.) Unfortunately, it is difficult to generate steeper wavetrains mechanically, since synchronous and subharmonic cross-waves are excited at the paddle (see Part 1).

Our experiments indicate that ripple wavetrains with $0.155 < \tau < 0.5$ ($6.4 < f < 9.8$ Hz) are stable to transverse and longitudinal modulations, as predicted by NLS equations (14) and (21) and by the fourth-order NLS equation of Hogan (1985). However, our experiments, when combined with the results of McGoldrick (1972), also show that all wavetrain frequencies between those for Wilton $n = 3$ and $n = 4$ ripples excite one of these internal resonances. Based on McGoldrick's more complete set of experiments, we suspect that the entire band of modulationally stable wavetrains is dominated by these internal resonances. In our experiment that excited Wilton $n = 3$ ripples, the third-harmonic wavetrain undergoes rhombus-quartet instabilities. In our experiment at the parametric boundary $\tau = 0.5$ ($f = 9.8$ Hz), which corresponds to Wilton $n = 2$ ripples, we find that both the 9.8 Hz wavetrain and the second-harmonic wavetrain undergo rhombus-quartet instabilities.

6. Epilogue

In this series of three experimental papers, we have examined the evolution of ripple wavetrains with small-to-moderate steepnesses ($\epsilon < 0.3$) within the analytical framework of RIT (resonant interaction theory). RIT supposes wave–wave interactions are weak so that nonlinear terms in the governing equations provide a small perturbation on the first-order (ϵ^1 or linear) motion and that resonant interactions dominate non-resonant interactions, which are neglected. Thereby, the magnitudes of interactions are rank-ordered, and a hierarchy of approximate

dynamical models, which are asymptotically valid in the limit $\epsilon \to 0$, is established. Usually, it remains for experimentalists to determine the actual numerical range of ϵ for which the hierarchial models are accurate, and that was one of our objectives. In experiments, viscous effects and measurement resolution impose a lower bound on ϵ that must be exceeded in order to observe resonant nonlinear interactions; however, it is the upper bound on ϵ that determines the robustness of the hierarchial models. Our search for an upper bound was not completely successful, owing to the inability of mechanical wavemakers to generate large-amplitude wavetrains without cross-wave contamination. But more importantly, we observed some ripple wavetrains for which *no* range of ϵ was found that allowed us to predict the outcome of an experiment using a straightforward application of hierarchial models from RIT.

According to RIT, the hierarchy of dynamical models begins with resonant three-wave interactions, then resonant four-wave interactions, and so on. In our experiments using ripple wavetrains with frequency f on clean, deep water, resonant triad interactions occur for $f > 19.6$ Hz and for the neighbourhood of $f = 9.8$ Hz, where a degenerate triad (internal resonance) occurs corresponding to Wilton $n = 2$ ripples. Resonant quartet interactions are possible for all frequencies, and a degenerate quartet occurs in the neighbourhood of $f = 8.4$ Hz corresponding to Wilton $n = 3$ ripples. Hence, resonant triads are expected to dominate wavetrain evolution for $f > 19.6$ Hz, and resonant quartets are expected to dominate wavetrain evolution for $f < 19.6$ Hz.

There is qualitative agreement between our experimental observations and RIT for wavetrains with $f < 19.6$ Hz. (We have not made a quantitative comparison.) In the neighbourhood of $f = 9.8$ Hz, we observed the degenerate triad corresponding to Wilson $n = 2$ ripples, and it was excited for $\epsilon \approx 0.04$, which is quite small. When nonlinearity was increased to $\epsilon \approx 0.10$, both the first- and second-harmonic wavetrains of this degenerate triad became unstable by (degenerate) rhombus-quartet interactions. In the neighbourhood of $f = 8.4$ Hz, we observed the degenerate quartet corresponding to Wilton $n = 3$ ripples, and it was excited for $\epsilon \approx 0.08$. When nonlinearity was increased to $\epsilon \approx 0.20$, the third-harmonic wavetrain was destabilized by rhombus-quartet interactions. Between 9.8 and 19.6 Hz rhombus-quartet interactions were dominant for all of the experimental wave steepnesses ($\epsilon \approx 0.15$–0.30).

There is qualitative disagreement between our experimental observations and RIT for wavetrains with $f > 19.6$ Hz. For these wavetrains evolution was observed to depend crucially on the nature of omnipresent, high-frequency, background waves (noise) whose amplitudes were exceedingly small and interactions with the test wavetrain were dynamically negligible according to RIT. If the high-frequency noise spectrum contained discrete component(s), a sequence of very small nonlinear interactions led to selective amplification of resonant triad(s) in the dynamically admissible low-frequency band of background waves. If the high-frequency noise spectrum was broad-banded, no resonant triads were selectively amplified. In the first case, the rhombus-quartet instability played an essential role on first-order effects, and in the second case, rhombus quartet interactions were the dominant first-order effect. These results persisted for all ϵ above the minimum needed to observe nonlinear interactions. These results suggest caution when using the hierarchial models of RIT to predict the dynamics of a weakly nonlinear system.

The authors gratefully acknowledge financial support provided by the Army

Research Office and the Office of Naval Research through the DoD University Research Instrumentation Program (grant number N00014-86-G-0201 with the University of Florida). The equipment purchased under this contract was essential in performing this research. The College of Engineering at the University of Florida has made significant contributions to the development of the research laboratory, and that support is gratefully acknowledged. We also wish to thank the Office of Naval Research for their continuing support under contract N00014-85-K-0201 at the University of Florida, M. P. would like to thank J. H. for the opportunity to work with him.

REFERENCES

ABLOWITZ, M. J. & SEGUR, H. 1979 On the evolution of packets of water waves. *J. Fluid Mech.* **92**, 691–715.

ABLOWITZ, M. J. & SEGUR, H. 1981 *Solitons and the Inverse Scattering Transform.* SIAM.

BENJAMIN, T. B. & FEIR, J. E. 1967 The disintegration of wave trains on deep water. Part 1. Theory. *J. Fluid Mech.* **27**, 417–430.

BENNEY, D. J. & NEWELL, A. C. 1966 The propagation of nonlinear wave envelopes. *J. Math. Phys. (Stud. Appl. Maths)* **46**, 133–139.

BENNEY, D. J. & ROSKES, G. 1969 Wave instabilities. *Stud. Appl. Maths* **48**, 377–385.

CHEN, B. & SAFFMAN, P. G. 1979 Steady gravity–capillary waves on deep water. I. Weakly nonlinear waves. *Stud. Appl. Maths* **60**, 183–210.

CHEN, B. & SAFFMAN, P. G. 1980 Steady gravity–capillary waves on deep water. II. Numerical results for finite amplitude. *Stud. Appl. Maths* **62**, 95–111.

CHEN, B. & SAFFMAN, P. G. 1985 Three-dimensional stability and bifurcation of capillary and gravity waves on deep water. *Stud. Appl. Maths* **72**, 125–147.

CHILDERS, D. & DURLING, A. 1975 *Digital Filtering and Signal Processing.* West Publishing Company.

CRAIK, A. D. D. 1985 *Wave Interactions and Fluid Flows.* Cambridge University Press.

CRAWFORD, D. R., LAKE, B. M., SAFFMAN, P. G. & YUEN, H. C. 1981 Stability of weakly nonlinear deep-water waves in two and three dimensions. *J. Fluid Mech.* **105**, 177–191.

DAVEY, A. & STEWARTSON, K. 1974 On three-dimensional packets of surface waves. *Proc. R. Soc. Lond.* A**338**, 101–110.

DJORDJEVIC, V. D. & REDEKOPP, L. G. 1977 On two-dimensional packets of capillary gravity waves. *J. Fluid Mech.* **79**, 703–714.

HASIMOTO, H. & ONO, H. 1972 Nonlinear modulation of gravity waves. *J. Phys. Soc. Japan* **33**, 805–811.

HENDERSON, D. 1986 Resonant interactions among ripples. MS thesis, Department of Engineering Sciences, University of Florida.

HENDERSON, D. & HAMMACK, J. 1987 Experiments on ripple instabilities. Part 1. Resonant triads. *J. Fluid Mech.* **184**, 15–41.

HENDERSON, D. & LEE, R. 1986 Laboratory generation and propagation of ripples. *Phys. Fluids* **29**, 619–624.

HOGAN, S. J. 1985 The fourth-order evolution equation for deep-water gravity–capillary waves. *Proc. R. Soc. Lond.* A **402**, 359–372.

LAKE, B. M., YUEN, H. C., RUNGALDIER, H. & FERGUSON, W. E. 1977 Nonlinear deep-water waves: Theory and experiment. Part 2. Evolution of a continuous wave train. *J. Fluid Mech.* **83**, 49–74.

LAMB, H. L. 1932 *Hydrodynamics.* Dover.

LIGHTHILL, M. J. 1965 Contributions to the theory of waves in non-linear dispersive systems. *J. Inst. Maths Applics* **1**, 269–306.

LONGUET-HIGGINS, M. S. 1978 The instabilities of gravity waves of finite amplitude in deep water. II. Subharmonics. *Proc. R. Soc. Lond.* A **360**, 489–505.

MA, Y.-C. 1979 The perturbed plane-wave solution of the cubic Schrödinger equation. *Stud. Appl. Maths* **60**, 43–58.

MA, Y.-C. 1982*a* On steady three-dimensional deep water weakly nonlinear gravity waves. *Wave Motion* **4**, 113–125.

MA, Y.-C. 1982*b* Weakly nonlinear steady gravity–capillary waves. *Phys. Fluids* **25**, 945–948.

MCGOLDRICK, L. F. 1972 On the rippling of small waves: a harmonic nonlinear nearly resonant interaction. *J. Fluid Mech.* **52**, 725–751.

MCLEAN, J. W. 1982*a* Instabilities of finite-amplitude water waves. *J. Fluid Mech.* **114**, 315–330.

MCLEAN, J. W. 1982*b* Instabilities of finite-amplitude gravity waves on water of finite depth. *J. Fluid Mech.* **114**, 331–341.

MCLEAN, J. W., MA, Y.-C., MARTIN, D. U., SAFFMAN, P. G. & YUEN, H. C. 1981 A new type of three-dimensional instability of finite amplitude gravity waves. *Phys. Rev. Lett.* **46**, 817–820.

MARTIN, D. U. & YUEN, H. C. 1980 Quasi-recurring energy leakage in the two-space dimensional nonlinear Schrödinger equation. *Phys. Fluids* **23**, 881–883.

MELVILLE, W. K. 1982 The instability and breaking of deep-water waves. *J. Fluid Mech.* **115**, 165–185.

MEIRON, D. I., SAFFMAN, P. G. & YUEN, H. C. 1982 Calculation of steady three-dimensional deep-water waves. *J. Fluid Mech.* **124**, 109–121.

MILES, J. W. 1984 Nonlinear Faraday resonance. *J. Fluid Mech.* **146**, 285–302.

PERLIN, M., HENDERSON, D. & HAMMACK, J. 1990 Experiments on ripple instabilities. Part 2. Selective amplification of resonant triads. *J. Fluid Mech.* **219**, 51–80.

PHILLIPS, O. M. 1977 *The Dynamics of the Upper Ocean.* 2nd edn. Cambridge University Press.

SAFFMAN, P. G. & YUEN, H. C. 1980*a* Bifurcation and symmetry breaking in nonlinear dispersive waves. *Phys. Rev. Lett.* **44**, 1097–1100.

SAFFMAN, P. G. & YUEN, H. C. 1980*b* A new type of three-dimensional deep-water wave of permanent form. *J. Fluid Mech.* **101**, 797–808.

SU, M.-Y. 1982 Three-dimensional deep-water waves. Part 1. Experimental measurement of skew and symmetric wave patterns. *J. Fluid Mech.* **124**, 73–108.

SU, M.-Y., BERGIN, M., MARLER, P. & MYRICK, R. 1982 Experiments on nonlinear instabilities and evolution of steep gravity–wave trains. *J. Fluid Mech.* **124**, 45–72.

WHITHAM, G. B. 1967 Non-linear dispersion of water waves. *J. Fluid Mech.* **27**, 399–412.

WILTON, J. R. 1915 On ripples. *Phil. Mag.* **29**(6), 688–700.

YUEN, H. C. & FERGUSON, W. E. 1978 Relationship between Benjamin–Feir instability and recurrence in the nonlinear Schrödinger equation. *Phys. Fluids* **21**, 1275–1278.

YUEN, H. C. & LAKE, B. M. 1982 Nonlinear dynamics of deep-water gravity waves. *Adv. Appl. Mech.* **22**, 67–229.

ZAKHAROV, V. E. 1968 Stability of periodic waves of finite amplitude on the surface of a deep fluid. *J. Appl. Mech. Tech. Phys.* (Engl. Transl.) **9**, 190–194.

ZAHKAROV, V. E. & SHABAT, A. B. 1972 Exact theory of two-dimensional self-focusing and one-dimensional self-modulation waves in nonlinear media. *Sov. Phys., J. Exp. Theor. Phys.* **65**, 997–1011.

ZHANG, J. & MELVILLE, W. K. 1987 Three-dimensional instabilities of nonlinear gravity–capillary waves. *J. Fluid Mech.* **174**, 187–208.